

Enhanced regional ocean ensemble data assimilation through atmospheric coupling in the SKRIPS model

Rui Sun ^{a,*}, Sivareddy Sanikommu ^b, Aneesh C. Subramanian ^c, Matthew R. Mazloff ^a, Bruce D. Cornuelle ^a, Ganesh Gopalakrishnan ^a, Arthur J. Miller ^a, Ibrahim Hoteit ^b

^a Scripps Institution of Oceanography, CA, USA

^b Physical Sciences and Engineering Division, King Abdullah University of Science and Technology (KAUST), Thuwal, Saudi Arabia

^c Department of Atmospheric and Oceanic Sciences, University of Colorado Boulder, CO, USA

ARTICLE INFO

Dataset link: https://github.com/iurnus/script_s_kaust_model, <https://zenodo.org/records/10408667>

Keywords:

Ocean Data Assimilation, DART, MITgcm, WRF, Red Sea

ABSTRACT

We investigate the impact of ocean data assimilation using the Ensemble Adjustment Kalman Filter (EAKF) from the Data Assimilation Research Testbed (DART) on the oceanic and atmospheric states of the Red Sea. Our study extends the ocean data assimilation experiment performed by Sanikommu et al. (2020) by utilizing the SKRIPS model coupling the MITgcm ocean model and the Weather Research and Forecasting (WRF) atmosphere model. Using a 50-member ensemble, we assimilate satellite-derived sea surface temperature and height and in situ temperature and salinity profiles every three days for one year, starting January 01 2011. Atmospheric data are not assimilated in the experiments. To improve the ensemble realism, perturbations are added to the WRF model using several physics options and the stochastic kinetic energy backscatter (SKEB) scheme. Compared with the control experiments using uncoupled MITgcm with ECMWF ensemble forcing, the EAKF ensemble mean oceanic states from the coupled model are better or insignificantly worse (root-mean-square errors are 23% to -1.3% smaller), especially when the atmospheric model uncertainties are accounted for with stochastic perturbations. We hypothesize that the ensemble spreads of the air-sea fluxes are better represented in the downscaled WRF ensembles when uncertainties are well accounted for, leading to improved representation of the ensemble oceanic states from the new experiments with the coupled model. This indicates the ocean model assimilation will be improved with coupled models and may relax the need for operational centers to provide atmospheric ensembles to drive ocean forecasts. Although the feedback from ocean to atmosphere is included in this two-way regional coupled configuration, we find no significant effect of ocean data assimilation on the ensemble mean latent heat flux and 10-m wind speed over the Red Sea. This suggests that the improved skill using the coupled model is not from the two-way coupling, but from downscaling the ensemble atmospheric forcings (one-way coupled) to drive the ocean model.

1. Introduction

Numerical models have been used to analyze and predict ocean states for decades. Realistically configured numerical models can simulate oceanic conditions that are generally consistent with observations, but there can be substantial differences when comparing with observations at specific times and locations (Edwards et al., 2015). Even with a perfect model, the differences can result from uncertainties of initial conditions, perturbations, parameterizations, and forcings. Because of this, data assimilation (DA) is used to constrain the model solutions using observational data, including accounting for observation uncertainty and model representational error (Edwards et al., 2015).

The Ensemble Kalman Filter (hereafter EnKF) provides an efficient framework for ocean data assimilation (Evensen, 1994). It has gained popularity because of its simple conceptual formulation and relative ease of implementation, requiring no derivation of tangent linear or adjoint models, with only forward model integration in time (Evensen, 2003). Furthermore, its computational requirements scale with ensemble size, and so can be affordable and comparable with other popular sophisticated assimilation methods (Evensen, 2003). EnKF based data assimilation systems have been developed for many applications. For example, Evensen and Van Leeuwen (1996) assimilated altimeter data in the Agulhas region using a quasi-geostrophic model; Sakov et al. (2012) and Hoteit et al. (2013) respectively produced realistic estimates of the ocean circulation in the North Atlantic and the Gulf of

* Corresponding author.

E-mail address: rus043@ucsd.edu (R. Sun).

Mexico; Sanikommu et al. (2020) investigated the impact of atmospheric forcing and model physics perturbations using an Ensemble Adjustment Kalman Filter (EAKF), which is a variant of EnKF (Anderson, 2001). In addition to ocean data assimilation, EnKF is used for operational atmospheric assimilation at the Canadian Meteorological Centre (Houtekamer et al., 2005) among many other applications (e.g., Lawson and Hansen, 2004; Leeuwenburgh et al., 2005; Bannister, 2017).

A major component of EnKF data assimilation systems is the background error covariance estimated from the ensembles (Bannister, 2008a,b; Song et al., 2010). EnKFs can suffer from the collapse of the ensemble spread, which unrealistically reduces the background error covariance in the sequential data assimilation system (e.g., Anderson and Anderson, 1999; Hoteit et al., 2002). This is because it is usually not practically possible for a realistic system with limited ensembles to account for all uncertainties. To mitigate this, covariance inflation techniques are used to increase the ensemble spread to better describe the background error covariance (Anderson and Anderson, 1999; Hoteit et al., 2002; Zhang et al., 2004; Whitaker and Hamill, 2012; Luo and Hoteit, 2012). A more representative approach is to account directly for uncertainties in the model, such as the forcing and boundary conditions. Diverse high-resolution forcings that represent the uncertainty of the atmosphere are indeed desirable for ocean ensemble data assimilation system. Many studies have demonstrated improved forecasts and analyses when driving ensemble ocean data assimilation systems with perturbed atmospheric forcing (Lisæter et al., 2003; Evensen, 2004; Wan et al., 2008; Shu et al., 2011; Sakov et al., 2012; Karspeck et al., 2013; Penny et al., 2015; Sanikommu et al., 2017, 2019). Others investigated the perturbed model physics (Sandery et al., 2014; Brankart et al., 2015; Lima et al., 2019), or combined the perturbations of atmospheric forcing and model physics (Vandenbulcke and Barth, 2015; Kwon et al., 2016; Sanikommu et al., 2020). A recent study by Sanikommu et al. (2020) performed a detailed analysis of the impacts of model physics perturbations and atmospheric forcing on a high-resolution regional ocean DA system. The DA experiments improved the forecasts of oceanic states by using multiple oceanic model physics and ensemble atmospheric forcing now available from operational weather systems.

Our study takes a step forward toward a fully coupled ocean-atmospheric data assimilation system, with application to the Red Sea region. A regional assimilation system is crucial for improving forecasts in the Red Sea due to its unique characteristics in terms of both oceanic and atmospheric conditions (Hoteit et al., 2021). The region is prone to dust and sandstorms, particularly during the transitional seasons of spring and autumn, originating from nearby deserts like the Sahara. These storms significantly reduce visibility and impact air quality (Prakash et al., 2014). The Red Sea also experiences frequent temperature inversions, especially in winter, which affect temperature profiles, pollutant dispersal, and vertical mixing of air masses. The region is influenced by two primary wind patterns: the Southwest Monsoon, bringing humid air and thunderstorms, and the Northwest Monsoon, bringing drier air (Langodan et al., 2017). A sea breeze often develops during the day, cooling coastal areas (Davis et al., 2019). The Red Sea warm surface waters contribute to high levels of water vapor, impacting local weather conditions and precipitation. The local atmospheric features vary significantly with seasons, weather patterns, and local geography (Dasari et al., 2021). The Red Sea holds economic importance and plays a vital role in international trade. Further, the Red Sea circulation plays a dominant role in modifying the salinity budgets of the western Indian Ocean. Global reanalysis often fails to capture the Red Sea circulation features accurately due to coarse resolutions and limited observations (Sanikommu et al., 2023a). Developing a high-resolution regional reanalysis using local observations and coupled ocean-atmospheric data assimilation system would greatly enhance the forecasts in the Red Sea, and this is important for many applications in this unique region.

In this context, we implement a new ensemble DA system for the Red Sea using the Scripps-KAUST Regional Integrated Prediction System (SKRIPS, Sun et al., 2019, 2023) and the Data Assimilation Research Testbed (DART, Anderson et al., 2009). This work is an extension of previous DA efforts for the Red Sea (Toye et al., 2017; Sanikommu et al., 2020, 2023a,b), replacing the uncoupled ocean model with the SKRIPS coupled model (Sun et al., 2019, 2023). Here we assimilate only oceanic observations using the DART-EAKF system and investigate the estimated oceanic and atmospheric states of the Red Sea regional coupled model. The ocean model physics are perturbed based on Sanikommu et al. (2020) to account for the uncertainties of the ocean states. The atmosphere model physics are also perturbed using different schemes. We evaluate the performance of the coupled model in forecasting the oceanic states, the impact of atmospheric model physics options on the coupled model, and the feedback of the ocean data assimilation to the atmospheric model. The atmospheric data are not assimilated here because it is beyond the scope of this work and the lateral boundary conditions from the ERA5 reanalysis constrain the atmosphere model. Although we only assimilate ocean observations in this work, the present study is a step toward developing a weakly coupled DA framework for the operational analysis and forecasting for the Red Sea. Because the random atmospheric states are generated by perturbing the model physics when using a coupled model, there is less need to generate large ensembles of atmospheric forcings (Sanikommu et al., 2023a), enhancing the robustness of the DA system.

The rest of the manuscript is organized as follows. We first introduce the ensemble DA system and its implementation in Section 2. The results of the DA experiments are presented and discussed in Section 3. The final section outlines the main findings and concludes this work.

2. Implementations and experimental design

2.1. The data assimilation framework

We use the SKRIPS model (Sun et al., 2019) for the coupled simulation: the oceanic model component is the MIT general circulation model (MITgcm, Marshall et al., 1997) and the atmospheric model component is the Weather Research and Forecasting (WRF) model (Skamarock et al., 2019). The Earth System Modeling Framework (ESMF, Hill et al., 2004) and the National United Operational Prediction Capability (NUOPC) layer are used to handle the coupling between MITgcm and WRF. The schematic diagram of the DART-SKRIPS framework and the domain used in the experiment are shown in Fig. 1. The ocean data are assimilated using EAKF available from the DART-MITgcm package (Hoteit et al., 2013, 2015), aiming to evaluate their impact on the ocean and atmosphere states in the coupled system. The ROCOTO workflow management system (Harrop et al., 2017) is used for automating the pre- and post-processing scripts in the newly developed DART-SKRIPS framework.

The coupled model is also described in the diagram shown in Fig. 1. In the coupling process, MITgcm sends sea surface temperature (SST) and ocean surface velocity to WRF; WRF sends air-sea flux and surface atmospheric fields to MITgcm, including (1) net surface longwave and shortwave radiative fluxes, (2) surface latent and sensible heat fluxes, (3) 10-m wind speed, (4) precipitation, and (5) evaporation. The MITgcm model uses the surface atmospheric variables to prescribe surface forcing, including (1) total net surface heat flux, (2) surface wind stress, and (3) freshwater flux. The total net surface heat flux is computed by adding surface latent heat flux, sensible heat flux, net shortwave radiation flux, and net longwave radiation flux. The surface latent and sensible heat fluxes are computed using the COARE 3.0 bulk algorithm in WRF (Fairall et al., 2003).

The data assimilation schemes used in this work follow our previous experiments (Sanikommu et al., 2020). In the forecast step, each model ensemble member is integrated forward in time from the last analysis step; then in the analysis step, the forecast ensemble members are

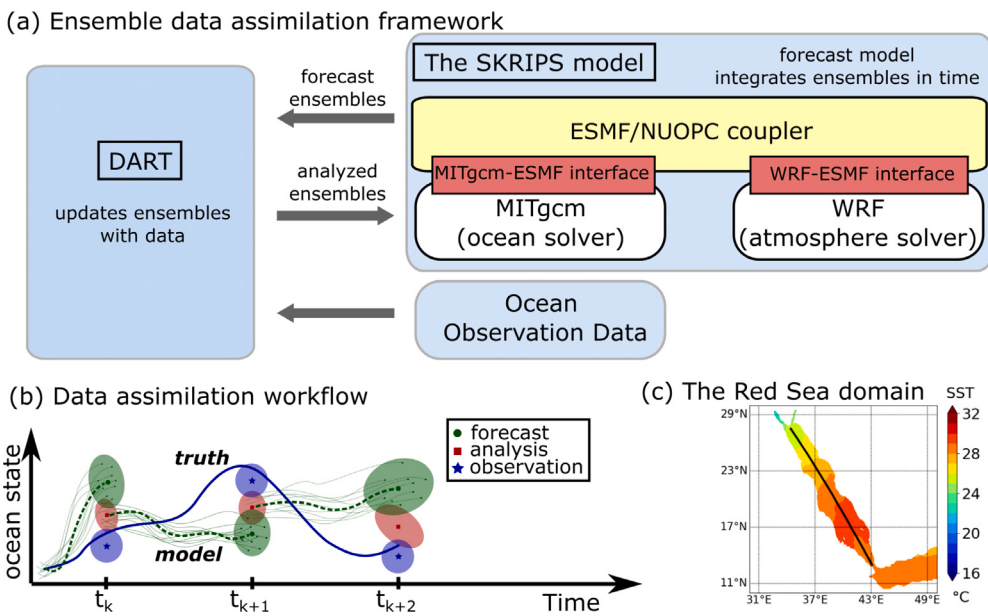


Fig. 1. The schematic description of the DART-SKRIPS data assimilation system. Panel (a) indicates the DART-SKRIPS framework: the blue blocks denote the SKRIPS model, DART, and ocean observations; the yellow block is the ESMF/NUOPC coupler; the white blocks are the ocean and atmosphere components; the red blocks are the implemented MITgcm-ESMF and WRF-ESMF interfaces. The arrows indicate the information exchange between DART and SKRIPS. Panel (b) shows the workflow at three time steps: the thick solid line indicates the evolution of the “truth”; the dashed line indicates the ensemble averaged forecast; the thin solid lines indicate the evolution of the ensemble members; the red dots indicate the analysis; the shaded areas indicate the error covariance; t_k , t_{k+1} , and t_{k+2} indicate three steps when observational data are assimilated. Panel (c) shows the domain of the coupled model, with the black line indicating the centerline of the Red Sea.

adjusted by the incoming observations using the Ensemble Adjustment Kalman Filter (EAKF). More details of the ensemble Kalman filter used in the present work can be found in Anderson (2001) and Toye et al. (2017).

2.2. Experimental design

To study the impact of ocean data assimilation on the oceanic and atmospheric states, we perform a series of 50-member ensemble DA experiments using coupled and uncoupled models starting from January 01 2011 to January 01 2012. The forecast period of our DA experiments is 3 days. After each forecast period, we assimilate the ocean observations to get the ocean analysis, then initialize the ocean model using the ocean analysis for the next forecast period. For the coupled model experiments, the ocean and atmosphere models are nested in GLORYS and ERA5 reanalyses, respectively. For the uncoupled model experiments, the ocean model is also nested in GLORYS, but driven by ECMWF derived atmospheric forcing. Further details on the initial and boundary conditions will be discussed in the latter sections. The same setup is used for the ocean model, but different options are used for the atmosphere in the 50-member ensemble DA experiments:

1. OCN.daO uses only the ocean model forced by the ECMWF ensemble mean.
2. OCN.daF uses only the ocean model forced by the 50-member ECMWF ensembles.
3. CPL.daO uses the coupled model with no perturbations to the atmosphere.
4. CPL.daS uses the coupled model with stochastic forcings in the atmospheric model.
5. CPL.daP uses the coupled model with perturbed physics options in the atmospheric model (e.g., microphysics, convection, and planetary boundary layer).
6. CPL.daSP uses the coupled model with stochastic forcings and perturbed atmosphere physics options.

OCN.daO and OCN.daF follow the experiments using the ocean-only models in Sanikommu et al. (2020). They also serve as benchmarks

to evaluate the performance of the coupled experiments, and we do not add inflation to the coupled and uncoupled experiments for consistency. In the coupled DA experiment CPL.daO, although we did not perturb the atmospheric model physics, the randomness of the atmospheric forcing is from the feedback of different ocean states. Different random number seeds are used for the stochastic model in CPL.daS and CPL.daSP from 1 to 50. The coupled DA experiments OCN.daS, OCN.daP, and OCN.daSP are conducted to assess the effect of different strategies of the atmospheric forcings, and thus we did not assimilate the atmospheric observational data in our experiments. The atmospheric response to the ocean is also important to study, but in this work, we aim to present the implementations of the DART-SKRIPS data assimilation framework. Hence we have not evaluated the sensitivity of the atmospheric state and its response to ocean DA by either running stand-alone WRF simulations or ocean DA experiments with atmospheric forcings from WRF models.

2.3. The forward models

The initial conditions, boundary conditions, and forcings for the forward models are outlined in Table 1. For the uncoupled experiments, the initial conditions are obtained from a spin-up run as described in Sanikommu et al. (2020), with randomly selecting 50 ocean states corresponding to ± 15 days from the initial time. The initial ensembles are sampled at 0000 UTC from the 15-year MITgcm model spin-up simulation. The boundary conditions for the ocean are updated by linearly interpolating between the daily data from Global Ocean Reanalysis and Simulation (GLORYS, Jean-Michel et al., 2021). To force the ocean in the uncoupled experiments, the atmospheric forcings are from the ECMWF atmospheric ensemble from The Observing System Research and Predictability Experiment Interactive Grand Global Ensemble project (TIGGE, Bougeault et al., 2010), with full details available in Buizza (2014). We combined the fields of the 00 and 12 UTC TIGGE initial conditions and 06 and 18 UTC forecasts as 6-hourly forcing for our ocean ensemble assimilation runs. For OCN.daO, we forced the model with the ensemble mean of the atmospheric forcings; for OCN.daF, we forced the model with the ECMWF 50-member ensembles.

Table 1

	OCN experiments	CPL experiments
Model region	10°N to 30°N; 30°E to 50°E	
Grid size	500 × 500	500 × 500 for ocean 125 × 125 for atmosphere
Grid spacing	0.04° × 0.04°	0.04° × 0.04° for ocean 0.16° × 0.16° for atmosphere
Microphysics scheme		Various (see Table 3)
Convection scheme		Various (see Table 3)
PBL scheme	Not necessary	Various (see Table 3)
Longwave radiation scheme		RRTMG
Shortwave radiation scheme		RRTMG
Land surface scheme		Noah land surface model
Vertical levels	50 (ocean only)	40 (atmosphere) 50 (ocean)
Initial and boundary conditions	GLORYS (ocean only)	ERA5 (atmosphere) GLORYS (ocean)
Atmospheric forcings for oceanic model	From ECMWF TIGGE product	From WRF

Table 2

Dictionary of the MITgcm model physics parameterizations in the present study. The parameterizations are randomly selected from this dictionary in the DA experiments.

Horizontal viscosity	Vertical Mixing	Horizontal Diffusion
Simple Harmonic (30 m ² /s)	K-Profile Parameterization	Implicit diffusion
Simple biharmonic (10 ⁷ m ⁴ /s)	PP81	Explicit diffusion (100 m ² /s)
SMAGLEITH-harmonic (30 m ² /s), Smag Coeff 2.5, and Leith Coeff 1.85	MY82	GMREDI-clipping (100 m ² /s)
	GGL90	GMREDI-dm95 (100 m ² /s) GMREDI-dd92 (100 m ² /s)

In the coupled experiments, the ocean initial and boundary conditions are identical to the uncoupled ones. All coupled experiments use the same initial and boundary conditions for the atmosphere model using ERA5 (ECMWF, 2017) reanalysis, with the lateral atmospheric boundary conditions updated by linearly interpolating between the 6-hourly fields. Spectral nudging is not used in the DA experiments because (1) nudging may constrain the high-frequency internal variability of the atmosphere model and (2) the domain size is comparable with wavelengths typically used in the spectral nudging simulations (Liu et al., 2012).

We choose the latitude-longitude (cylindrical equidistant) map projection to generate the grids for MITgcm and WRF. The domains for both models extend from 10°N to 30°N and from 30°E to 50°E. In the ocean model, the horizontal grid has 500 × 500 (lat×long) cells and the spacing is about 4 km; in the atmospheric model, the horizontal grid has 125 × 125 (lat×long) cells and the spacing is about 16 km. Because the atmospheric model is far more computationally expensive than the ocean model (Sun et al., 2019), we used a lower resolution due to limited computational resources. There are 40 sigma layers in the atmospheric model (top pressure is 50 hPa) and 50 z-layers in the ocean model (dz = 4 m at the top). The time step of the oceanic model is 200 s; the time step of the atmospheric model is 25 s; the coupling interval is 200 s.

2.4. Model perturbations

For the oceanic simulations in all DA experiments, we use various physical parameterization schemes to account for the effects of unresolved scales of motion as proposed by Sanikommu et al. (2020), summarized in Table 2. Three different categories of model physics are selected: horizontal viscosity, vertical mixing, and horizontal diffusion. We include three different horizontal viscosity schemes: the simple harmonic scheme, the simple biharmonic of Holland (1978), and the Smagorinsky/Leith scheme (Smagorinsky et al., 1993; Griffies and

Hallberg, 2000) with the coefficients suggested in the literature (Leith, 1996; Griffies and Hallberg, 2000). For vertical mixing, four different schemes are included: the nonlocal K-Profile Parameterization (KPP) scheme (Large et al., 1994), the PP81 scheme (Pacanowski and Philander, 1981), the MY82 scheme (Mellor and Yamada, 1982), and the GGL90 scheme (Gaspar et al., 1990). For the horizontal diffusion, we use implicit diffusion, simple-explicit harmonic diffusion, and three different flavors of Gent-McWilliams/Redi subgrid-scale eddy parameterization schemes (hereafter GMREDI, Gent and McWilliams, 1990; Gent et al., 1995; Redi, 1982): the GMREDI clipping scheme of Cox (1987), the GMREDI-dm95 tapering scheme of Danabasoglu and McWilliams (1995), and the GMREDI-dd92 tapering scheme of Large et al. (1997). Table 2 lists the coefficients used in these schemes. Although perturbing the coefficients is a possible option to generate the ensembles, Sanikommu et al. (2020) demonstrated that using random parameterization schemes is an effective way to generate the perturbations.

We also perturb the physics options in WRF to parameterize micro-physics, convection, and planetary boundary layer (PBL), summarized in Table 3. For the microphysics we use the Morrison 2-moment scheme (Morrison et al., 2009), the Purdue-Lin scheme (Chen and Sun, 2002), the Thompson scheme (Thompson et al., 2008), the WRF single moment 6-class scheme (Hong and Lim, 2006), and the WRF double moment 6-class scheme (Lim and Hong, 2010). For the cumulus convection, we use the Kain-Fritsch scheme (Kain, 2004), the Betts–Miller–Janjic scheme (Janjić, 1994), the Grell–Freitas Ensemble scheme (Grell and Freitas, 2014), the new Tiedtke scheme (Zhang and Wang, 2017), and the simplified Arakawa–Schubert scheme (Kwon and Hong, 2017). For the planetary boundary layer, we use the Mellor–Yamada Nakanishi Niino scheme (MYNN, Nakanishi and Niino, 2004, 2009), the Yonsei University scheme (Hong et al., 2006), and the Mellor–Yamada–Janjic scheme (Janjić, 1994). The radiation and land surface schemes are not perturbed: the Rapid Radiation Transfer Model

Table 3

Dictionary of WRF model physics parameterizations in the present study. The physics options used in the experiments without perturbing the model physics (i.e., CPL.daO and CPL.daS) are highlighted using bold red color. In other experiments, the parameterizations are randomly selected from this dictionary.

Microphysics	Convection	Planetary boundary layer
Morrison 2-moment	Kain–Fritsch	Mellor–Yamada Nakanishi Niino
Purdue-Lin	Betts–Miller–Janjic	Yonsei University
Thompson	Grell–Freitas Ensemble	Mellor–Yamada–Janjic
WRF single moment 6-class	New Tiedtke	
WRF double moment 6-class	Simplified Arakawa–Schubert	

for GCMs (RRTMG, Iacono et al., 2008) is used for longwave and short-wave radiation transfer through the atmosphere; the Noah land surface model is used for the land surface processes (Tewari et al., 2004). The physics scheme perturbation is based on the ensemble forecast system of the Center For Western Weather and Water Extremes (CW3E, Oakley et al., 2023). For the experiments without perturbing the atmospheric model (i.e., CPL.daO and CPL.daS), we use Morrison 2-moment scheme, Kain–Fritsch scheme, and MYNN scheme for microphysics, convection, and PBL, respectively.

In addition to perturbing the atmospheric model physics, we used the SKEB scheme (Shutts, 2005; Berner et al., 2009) to account for the unrepresented uncertainties in the model. This scheme adds stochastic, small-amplitude perturbations to the horizontal wind and potential temperature. The default amplitudes of the stochastic perturbations in WRF were used in CPL.daS and CPL.daSP, which were able to provide more reliable ensemble spreads (Berner et al., 2011, 2015).

2.5. Data used in assimilation and validation

We assimilate data from level-4 SST blended daily product available on a $0.25^\circ \times 0.25^\circ$ grid (Reynolds et al., 2007; Banzon et al., 2016), along-track satellite altimeter level-3 sea level anomalies (SLAs; corrected for dynamic atmospheric loading, ocean tide, and long wavelength errors) available from Copernicus Marine Environment Monitoring Service (here after CMEMS-L3, Mertz et al., 2017), and quality controlled in situ glider temperature and salinity profiles from EN4 data (Ingleby and Huddleston, 2007; Good et al., 2013). The in situ temperature and salinity profiles are sparse, and there are only 244 temperature and 110 salinity profiles in the entire year 2011 from the glider in the Red Sea. Errors associated with these observations are assumed uncorrelated, so the observational error covariance matrix is diagonal. The combined observation and representation error variance is determined based on previous DA experiments (Toye et al., 2017; Sanikommu et al., 2020) and accounts for errors due to: measurement devices, omitted processes, unresolved subgrid scale dynamics, and numerical errors in interpolation. Temporally static, partially homogeneous, and depth independent observational error variance values of $(0.5^\circ\text{C})^2$, $(0.04\text{ m})^2$, $(0.5^\circ\text{C})^2$, and $(0.3\text{ psu})^2$ are then used for satellite SST, satellite along-track SLA, in situ temperature and salinity, respectively. A cutoff radius of 300 km was imposed to localize the impact of observations in the horizontal direction (no vertical localization is used) to mitigate spurious long-distance correlations.

To validate the DA experiments, we first use the above-mentioned assimilated data to examine the innovations and residuals, and then we use other available data to compare with the obtained forecasts and analyses. To further analyze the subsurface features, we use 206 profiles of temperature and salinity collected between September 15 to October 08 2011 by a joint Woods Hole Oceanographic Institution (WHOI) and King Abdullah University of Science and Technology (KAUST) cruise, sampled with a horizontal spacing of 10 km (Zhai et al., 2015). We also use other satellite products to evaluate the DA results. For SST we select the high-resolution daily averaged level 4 SST product from the Operational Sea Surface Temperature and Sea Ice Analysis (OSTIA, Stark et al., 2007; Donlon et al., 2012) because it is mapped differently with higher resolution. For sea surface height (SSH) we use multitemission

altimeter merged satellite level 4 gridded absolute dynamic topography (ADT) provided by CMEMS (hereafter CMEMS-L4, Mertz et al., 2017). It should be noted that the OSTIA SST and CMEMS-L4 SSH are not completely independent from the assimilated data, but they are still useful for testing the implementation of the DA system. The OSTIA SST is mapped differently with higher resolution compared with the assimilated OISST. The CMEMS-L4 data is mapped on a 0.25° grid and thus can be used to validate analyses and forecasts across the entire Red Sea region compared with the along-track data CMEMS-L3. Because of the lack of in situ observational data of the atmosphere, we use ERA5 to validate the latent heat fluxes and wind speed simulated by the coupled experiments.

The SSH data are pre-processed following Sanikommu et al. (2020) before being assimilated in the coupled model. We first get the time-averaged SSH from the 15-year MITgcm model spin-up simulation, then the SSH anomaly from the DA experiments is the instantaneous SSH obtained in the simulations minus the time-averaged SSH. On the other hand, the SSH anomalies in CMEMS-L3 and CMEMS-L4 are the sea level height above the mean surface based on the long-term averaged observations between 1993 to 2012.

3. Results

The results obtained from the DA experiments are presented in this section. First, we analyze the ensemble spread of the atmospheric forcings and sea surface temperature. Then we examine the ocean states (e.g., SST, SSH, and vertical profiles) to assess the impact of atmospheric forcings in the uncoupled and coupled systems using the validation data. In addition to the ocean states, the air-sea exchanges (e.g., latent heat flux) and surface atmospheric states (e.g., wind speed) are also analyzed to illustrate the feedback from the ocean to the atmosphere due to assimilation. Finally, we discuss the changes in the ocean dynamics from assimilating the observation data.

3.1. Ensemble spread analysis

We first demonstrate the ensemble model spread obtained in the DA experiments. Figs. 2 and 3 display the temporal evolution of atmospheric forcing root-mean-square (RMS) spread in the DA experiments, except for OCN.daO which is forced by the ECMWF ensemble mean that does not have any ensemble spread in the atmospheric forcing. The spread in OCN.daF is from the ECMWF ensemble atmospheric forcing; others are from the coupled model outputs. In comparison with OCN.daF, the spread in CPL.daO is smaller by about one order of magnitude because the atmospheric models are not perturbed and the spread of atmosphere is from the ocean perturbations. When the SKEB scheme is applied in CPL.daS and CPL.daSP, the spread of the atmospheric forcing is larger than that in OCN.daF, which in turn increases the SST spread, shown in Fig. 4. Similar to Sanikommu et al. (2020), we hypothesize that accounting for the uncertainties in various sources will lead to a better representation of the background (forecast) error covariance and improve the ocean state forecasts. The oscillations of the SST spread during July and August can be attributed to the large variations of the atmospheric model during the strong Tokar jet, a southern Red Sea strong wind jet that blows from the African continent through the Tokar Mountain Gap (Sanikommu et al., 2020).

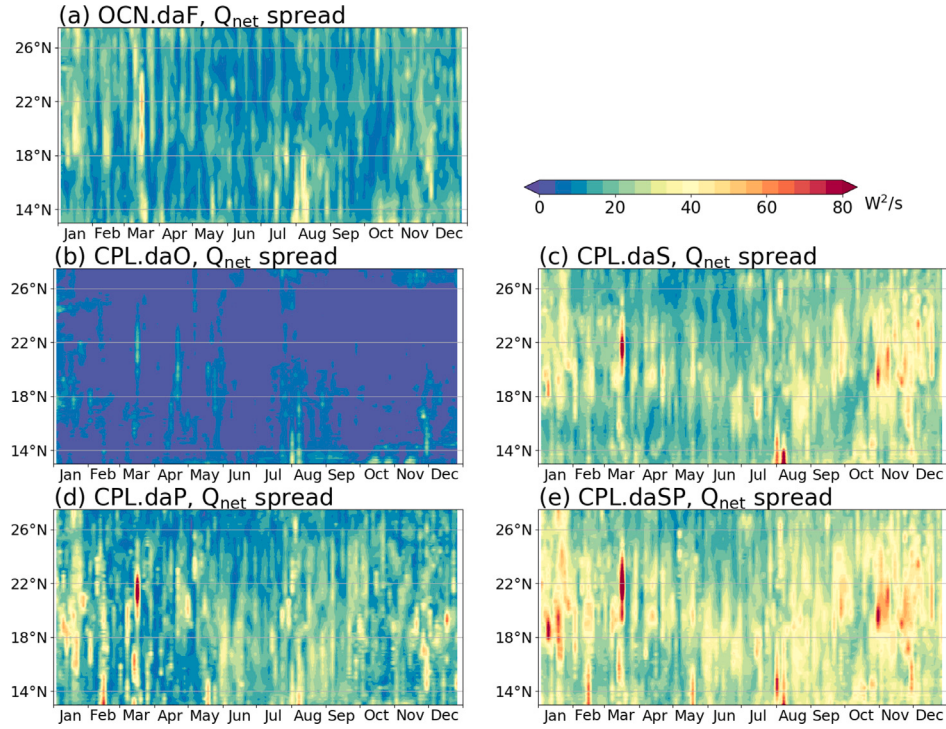


Fig. 2. The spatial and temporal evolution of the RMS spread of net surface heat flux Q_{net} along the center line of the Red Sea shown in Fig. 1(c). The Q_{net} is calculated by summing up the latent heat flux, sensible heat flux, net surface shortwave fluxes, and net surface longwave fluxes. Panel (a) shows the spread in the ocean-only experiment driven by ECMWF derived forcing; Panel (b–e) show the spread in the coupled experiments with no perturbations, only SKEB, only perturbed model physics, and SKEB + perturbed model physics, respectively.

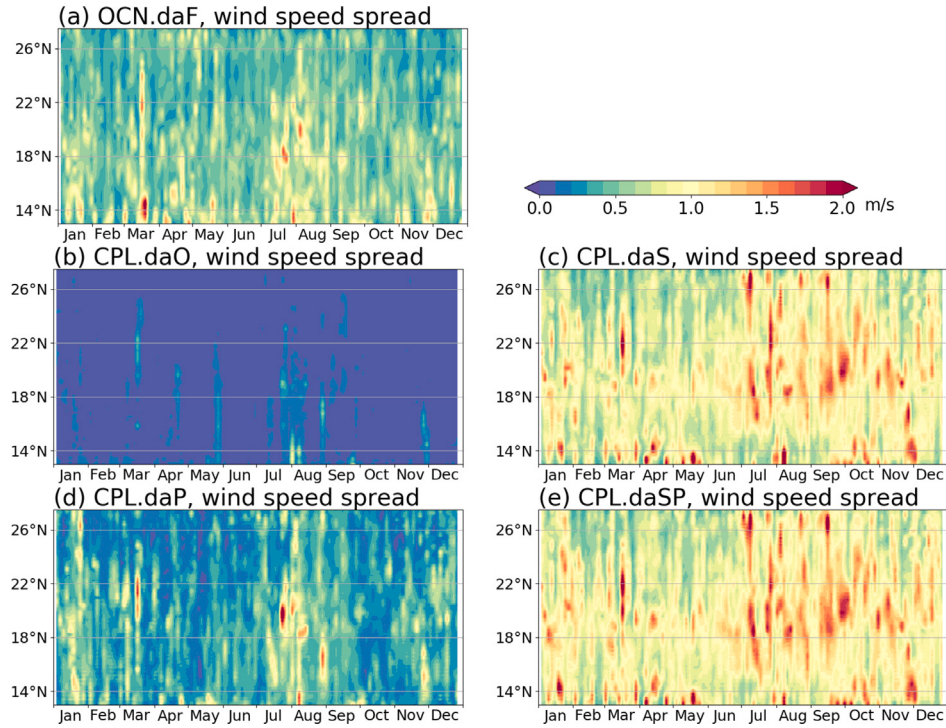


Fig. 3. The spatial and temporal evolution of the RMS spread of 10-m wind speed along the center line of the Red Sea shown in Fig. 1(c). Panel (a) shows the spread from the ECMWF derived forcing; Panel (b–e) show the spread in the coupled experiments with no perturbations, only SKEB, only perturbed model physics, and SKEB + perturbed model physics, respectively.

The ocean forecasts and the impact of the atmospheric forcings on the ocean states will be detailed in the latter sections. Note that because the model error covariance matrix is very large in this case, we present

the ensemble spread as a proxy for covariance structure and magnitude in the ensemble. A discussion of the model error covariance matrix can be found in Appendix A.

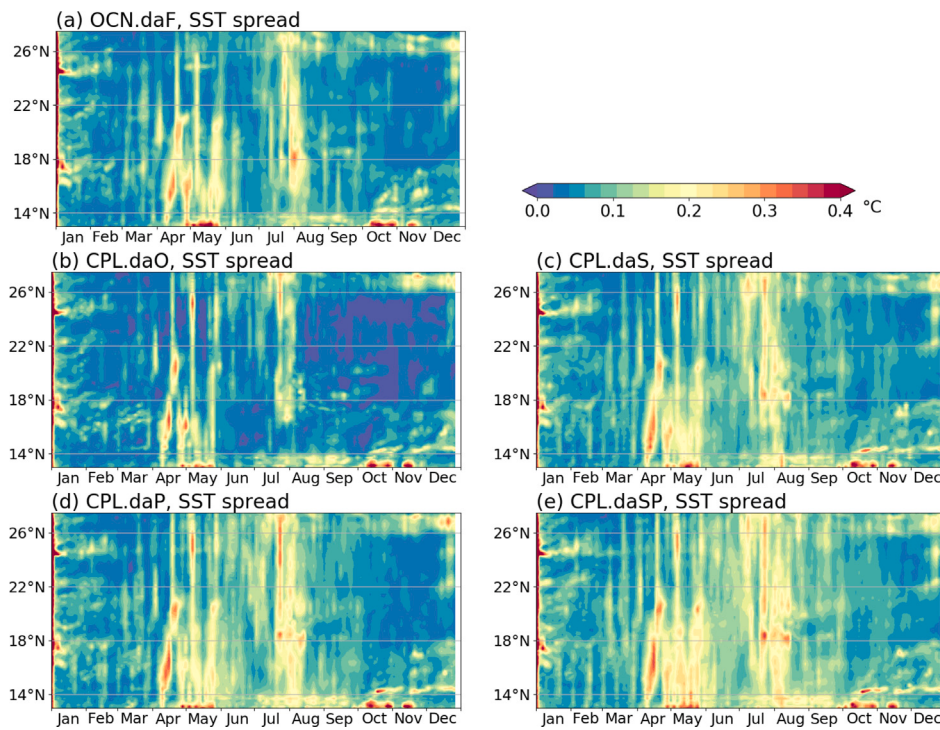


Fig. 4. The spatial and temporal evolution of the RMS spread of Sea Surface Temperature along the center line of the Red Sea shown in Fig. 1(c). Panel (a) shows the spread in the ocean-only experiment driven by ECMWF derived forcing; Panel (b–e) show the spread in the coupled experiments with no perturbations, only SKEB, only perturbed model physics, and SKEB + perturbed model physics, respectively.

3.2. Sea surface temperature

We analyze the SST obtained in our DA experiments to assess its sensitivity to the atmospheric perturbations. The root-mean-square-errors (RMSEs) between the SST analyses and the assimilated observations in all DA experiments are shown in Fig. 5 and summarized in Table 4. The best SST forecast and analysis are both from experiment CPL.daSP, when the SKEB scheme is turned on and the WRF physics options are perturbed. The SSTs obtained in the coupled experiments (CPL.daS, CPL.daP, and CPL.daSP; except for the benchmark case CPL.daO) are better than that of the uncoupled experiment OCN.daF, with improvements more than twice larger than standard error of the mean SST from CPL.daSP (about 0.015°C, the standard deviation of SST divided by the square-root of the number of ensemble members). Better improvements are obtained when using only the stochastic forcings (CPL.daS) compared with only perturbing the WRF physics (CPL.daP), but this difference is less significant (smaller than 0.015°C). We hypothesize that when we perturb the ocean and atmosphere model in our experiments, we better consider the uncertainties in the models, leading to a better background error estimate in the assimilation. This leads to improved forecasts and analyses of the ocean states in our experiments.

Fig. 5 shows that the RMSEs of SST forecasts and analyses increase in summer for the benchmark runs (i.e., OCN.daO and CPL.daO), but RMSEs get smaller when using the coupled model (i.e., CPL.daS, CPL.daP, and CPL.daSP). In this season, the SST has a larger spread in all the experiments, similar to the results shown in Sanikommu et al. (2020), likely because the ocean is more sensitive to heat fluxes when the mixed layer depth is shallower. It is also noted that the SST initial spread is high based on the sampling of model states from the long-term MITgcm spin-up simulation, but decreases quickly in the DA experiments within a few assimilation cycles. This may indicate the SST variability from the sampled model fields of long-term MITgcm simulation is high for starting time of assimilation (January 01, 2011), which is in consistent with Karnauskas and Jones (2018), Fig 5f. This

high initial SST spread deserves further investigation using sampling different from Sanikommu et al. (2020) in future work.

In addition to the assimilated data, we validated the SSTs using the OSTIA SST. Although the OSTIA SST is not completely independent from the assimilated data, it does provide a metric for evaluating the performance of the implemented DA framework. The RMSEs and correlations are shown in Fig. 6 and summarized in Table 4. We present the SST correlations to evaluate the forecast of the SST evolution during the year. It can be seen that the SST obtained in CPL.daSP has larger correlations and smaller RMSEs in the north Red Sea, center Red Sea, and Gulf of Aden regions. Compared with the uncoupled experiment OCN.daF, the forecasts in CPL.daSP has a smaller RMSE by 0.035°C (6.1%). On the other hand, the SST analysis obtained in CPL.daSP has a slightly larger RMSE compared to that obtained in CPL.daF, but the differences between OCN.daF, CPL.daS, CPL.daP, and CPL.daSP are within 0.01°C (2%). It should be noted that when comparing with OSTIA data the differences between the DA experiments are getting smaller, which is because of the bias between the OSTIA SST and assimilated data. In addition, the CPL.daSP also has the smallest distance between the forecasts and analyses RMSEs, indicating less “assimilation shock” and more balanced ocean states in the DA experiment.

3.3. Sea surface height

The SSH fields as estimated in the DA experiments compared with the assimilated data are presented in Fig. 7 and Table 5. Similar to the SST results, the coupled DA experiments exhibit smaller RMSE and larger spread. The SSH forecast errors in OCN.daF, CPL.daS, CPL.daP, and CPL.daSP are not significantly different. Although CPL.daSP still has the smallest RMSEs, the differences are within 2% and smaller than the standard errors (about 0.001 m). For the SSH analyses, on the other hand, the CPL.daS and CPL.daSP are more significantly improved (RMSEs are smaller by 10% compared with OCN.daF and CPL.daP) when

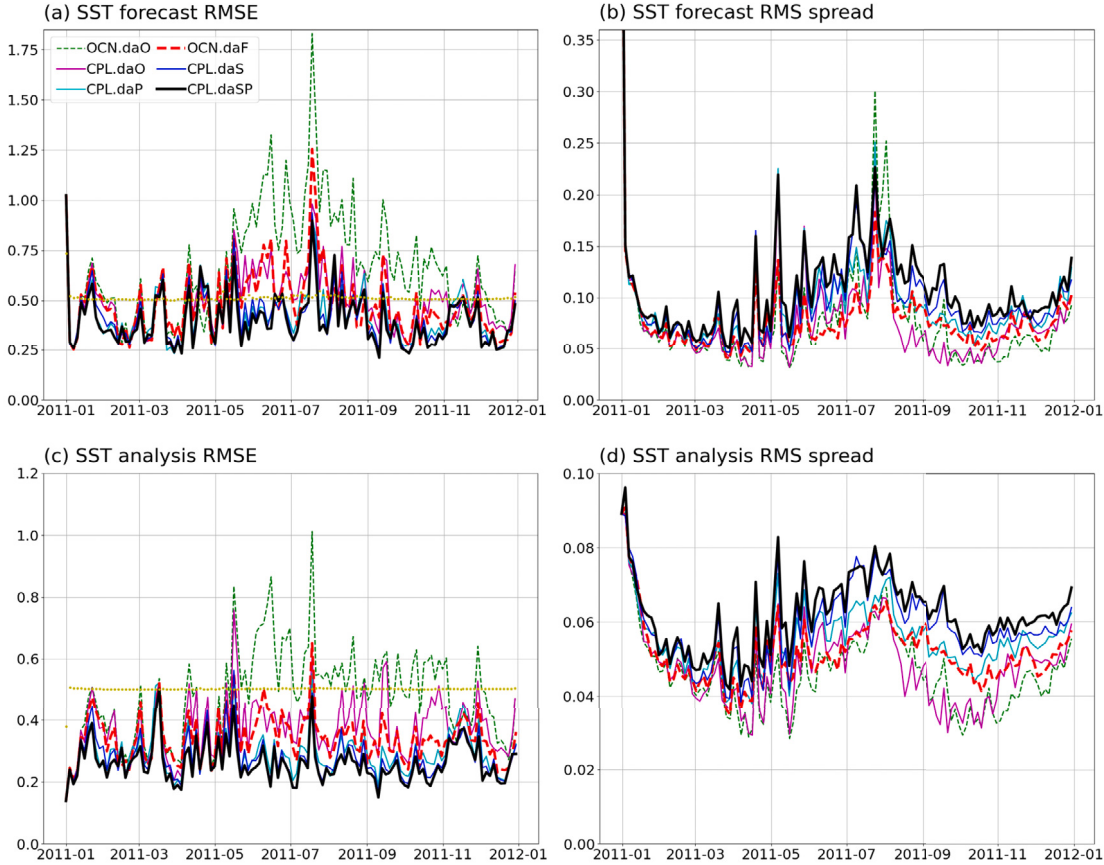


Fig. 5. Time history of SST RMSEs and spreads during the data assimilation experiment. Panels (a) and (c) show the RMSEs of the forecasts and analyses against the assimilated data; Panels (b) and (d) show the spread of SST in the forecasts and analyses. The yellow dots in Panels (a) and (c) indicate the total uncertainty (square root of the sum of ensemble variance and observational variance (0.5°C^2)) of CPL.daSP.

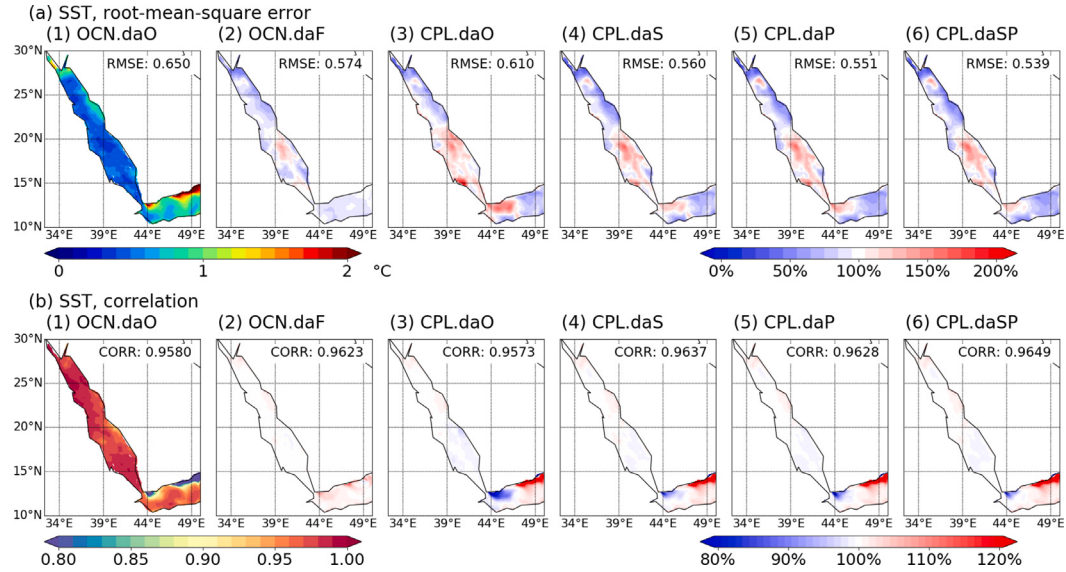


Fig. 6. SST RMSEs and correlations obtained in the DA experiments validated against OSTIA. Panels (a) and (b) show the RMSE and correlation of the “forecast” SST. The contours in column 1 are the RMSEs of OCN.daO experiment in comparison with OSTIA data; columns 2–6 are the RMSEs obtained in other experiments normalized by those obtained in OCN.daO to highlight differences, showing the ratios in percentage.

SKEBS are used, suggesting that including the stochastic forcing in model parameters is the key for improvements. We hypothesize that the improvements of the ensemble forcing improves the background error

estimate for the DA experiments. Note that the spread of surface wind forcing shown in Fig. 3 is greatly increased when using the stochastic forcing.

Table 4

Summary of SST obtained in the DA experiments against the validation data. The relative differences between CPL.daSP and OCN.daF are listed in the parenthesis behind the CPL.daSP results.

	OCN.daO	OCN.daF	CPL.daO	CPL.daS	CPL.daP	CPL.daSP
SST RMSE against assimilated data						
Forecast	0.656	0.486	0.500	0.419	0.426	0.403 (-17%)
Analysis	0.475	0.341	0.374	0.281	0.294	0.262 (-23%)
SST RMSE against OSTIA data						
Forecast	0.650	0.574	0.610	0.560	0.551	0.539 (-6.1%)
Analysis	0.486	0.463	0.484	0.468	0.472	0.469 (+1.3%)
SST correlation with OSTIA data						
Forecast	0.9580	0.9623	0.9573	0.9637	0.9628	0.9649 (+0.27%)
Analysis	0.9786	0.9805	0.9773	0.9800	0.9788	0.9791 (-0.14%)
SST spread						
Forecast	0.078	0.080	0.077	0.098	0.095	0.108 (+35%)
Analysis	0.046	0.052	0.048	0.059	0.055	0.062 (+19%)

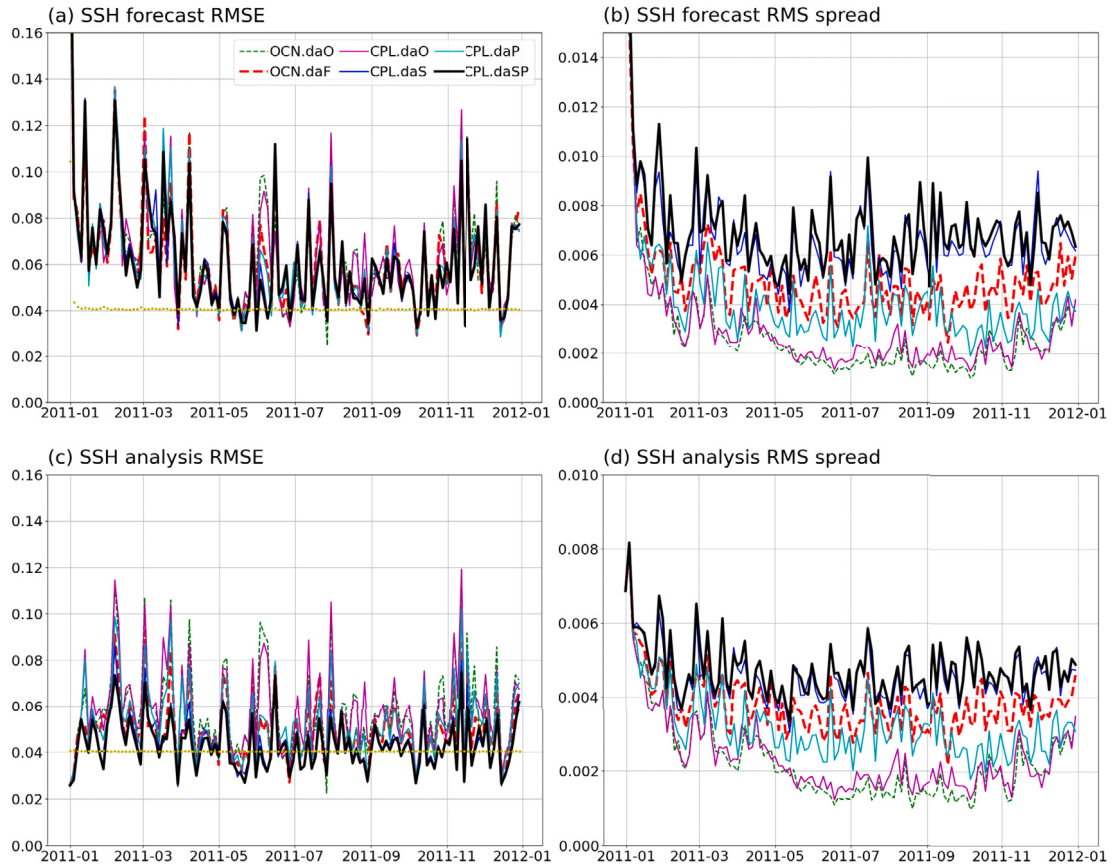


Fig. 7. Evolution of the SSH RMSEs and spreads during the data assimilation experiment. Panels (a–b) show the RMSEs of the forecasts and analyses against the assimilated data; Panels (c–d) show the RMS spread of SSH in the forecasts and analyses. The yellow dots in Panels (a) and (c) indicate the total uncertainty (square root of the sum of ensemble variance and observational variance (0.04 m^2)) of CPL.daSP.

The temporal evolution of the SSH is also examined by comparing with CMEMS-L4 data to test our DA implementations, shown in Fig. 8. Here we only highlight the differences of the SSH analyses because the forecasts are close to each other. Fig. 8 shows that the CPL.daSP experiment has larger correlations and smaller RMSEs in both the Red Sea and the Gulf of Aden regions. Similar to the results shown in Fig. 7, when using the stochastic forcings in WRF, CPL.daS and CPL.daSP outperform the uncoupled model OCN.daF (see Table 5).

3.4. Temperature and salinity profiles

In our DA experiments, we assimilate the quality-controlled in situ glider data from EN4, with 244 temperature profiles and 110 salinity profiles. The subsurface features of the ocean are validated against independent (i.e. not assimilated) CTD observations of temperature and salinity from the WHOI/KAUST summer cruise in the Red Sea between September 15 and October 08 2011. The difference between daily averaged forecasts and observations is shown in Figs. 9 and 10. For the

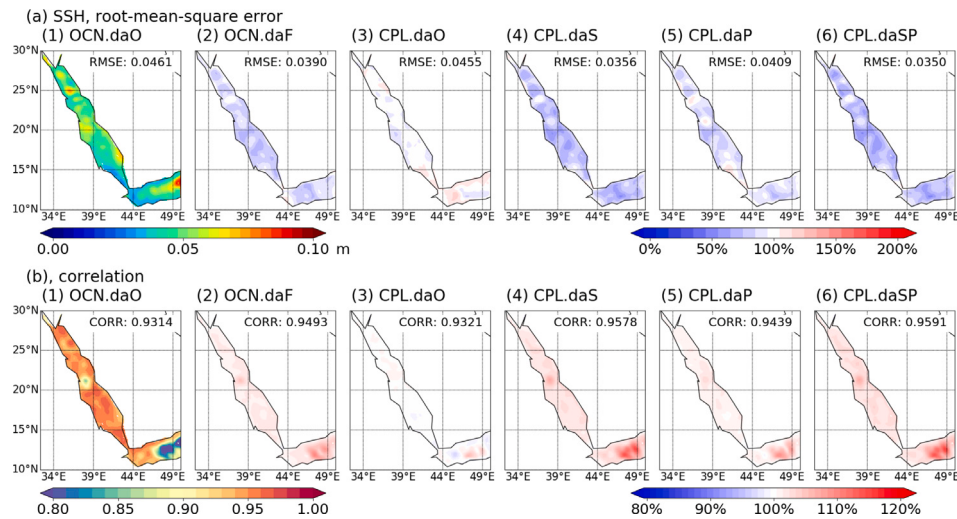


Fig. 8. SSH RMSEs and correlations obtained in the DA experiments validated against CMEMS-L4 data. Panels (a) and (b) show the RMSEs and correlations of the SSH analyses. The contours in column 1 are the RMSEs of OCN.daO experiment in comparison with CMEMS-L4 data; columns 2–6 are the RMSEs obtained in other experiments normalized by those obtained in OCN.daO to highlight differences, showing the ratios in percentage.

Table 5

Summary of SSH obtained in the DA experiments against the validation data. The relative differences between CPL.daSP and OCN.daF are listed in the parenthesis behind the CPL.daSP results.

	OCN.daO	OCN.daF	CPL.daO	CPL.daS	CPL.daP	CPL.daSP
SSH RMSE against assimilated data						
Forecast	0.0646	0.0626	0.0650	0.0624	0.0626	0.0620 (-0.96%)
Analysis	0.0580	0.0495	0.0578	0.0446	0.0522	0.0433 (-12.5%)
SSH RMSE against CMEMS-L4 data						
Forecast	0.0513	0.0486	0.0513	0.0483	0.0494	0.0482 (-0.82%)
Analysis	0.0461	0.0390	0.0455	0.0356	0.0409	0.0350 (-10.3%)
SSH correlation against CMEMS-L4 data						
Forecast	0.9121	0.9197	0.9109	0.9197	0.9168	0.9204 (+0.07%)
Analysis	0.9314	0.9493	0.0320	0.9578	0.9439	0.9590 (+1.0%)
SSH spread						
Forecast	0.0034	0.0056	0.0036	0.0073	0.0048	0.0076 (+36%)
Analysis	0.0023	0.0038	0.0024	0.0046	0.0032	0.0047 (+23%)

surface of the ocean between 0–20 m, the errors of the temperature are smaller in all experiments compared with OCN.daO, which is consistent with the SST errors shown in Fig. 6. More than 2 degree and 0.8 psu differences are found for temperature and salinity profiles in the thermocline between 50–100 m. For the temperature profiles, the RMSE in CPL.daSP (0.361°C) is smaller than OCN.daO (0.408°C) by about 10%, especially near the ocean surface, but within 2% difference compared to OCN.daF, CPL.daO, and CPL.daS. For the salinity profiles, the forecast RMSE of CPL.daSP (0.082 psu) is smaller than the benchmark experiment OCN.daO by about 30%. It is noted that CPL.daP has the smallest RMSE for temperature (0.344°C), but its salinity RMSE is significantly larger (0.122 psu) than CPL.daSP. Compared with the ocean-only experiment OCN.daF, the RMSEs in CPL.daS and CPL.daSP are not significantly different (within 1% or 2%). The relative differences of the temperature and salinity profiles are detailed in Appendix B. Although the coupled experiment is no better than the best uncoupled experiment OCN.daF, the results indicate the stochastic schemes in WRF are crucial for producing better forecasts of the ocean profiles.

3.5. Feedback to the atmosphere

We compare the atmospheric surface variables obtained in the DA experiments to assess the impact of ocean data assimilation on the surface of the atmosphere. We compare the latent heat fluxes and 10-m wind speed obtained in the DA experiments to evaluate the ocean

feedback to the heat and momentum fluxes. We use ERA5 as a reference and present the RMSEs of latent heat fluxes and 10-m wind speed from assimilation experiments in Fig. 11. Here we only compare the data on the centerline of the Red Sea to highlight ocean regions. It can be seen that the RMSEs do not grow significantly with time, showing the capability of the coupled system for the 1-year DA experiments. We hypothesize this is because the atmospheric states are constrained by the boundary conditions for this relatively small domain. Compared with the RMSEs of latent heat flux and 10-m wind speed in the benchmark case CPL.daO (62.9 W/m² and 1.52 m/s), the CPL.daSP (60.2 W/m² and 1.47 m/s) has smaller errors by about 4%, but the RMSE differences are smaller than the standard error (3.1 W/m² and 0.09 m/s), implying the improved ocean states may not significantly impact the atmospheric states. Because of the small differences in the surface atmosphere, this indicates that for the Red Sea region, the skill of the coupled model is not from the two-way coupling, but from the atmospheric forcings in the down-scaled WRF ensembles (one-way coupled) to drive the ocean model.

3.6. Vertical current speed

Toye et al. (2017) argued that the dynamical balances (or assimilation shock) in the oceanic model from the EAKF increments increase the spread of the Red Sea forecasts. The imbalances are also reported in other EAKF assimilation experiments (Anderson et al., 2000; Hoteit

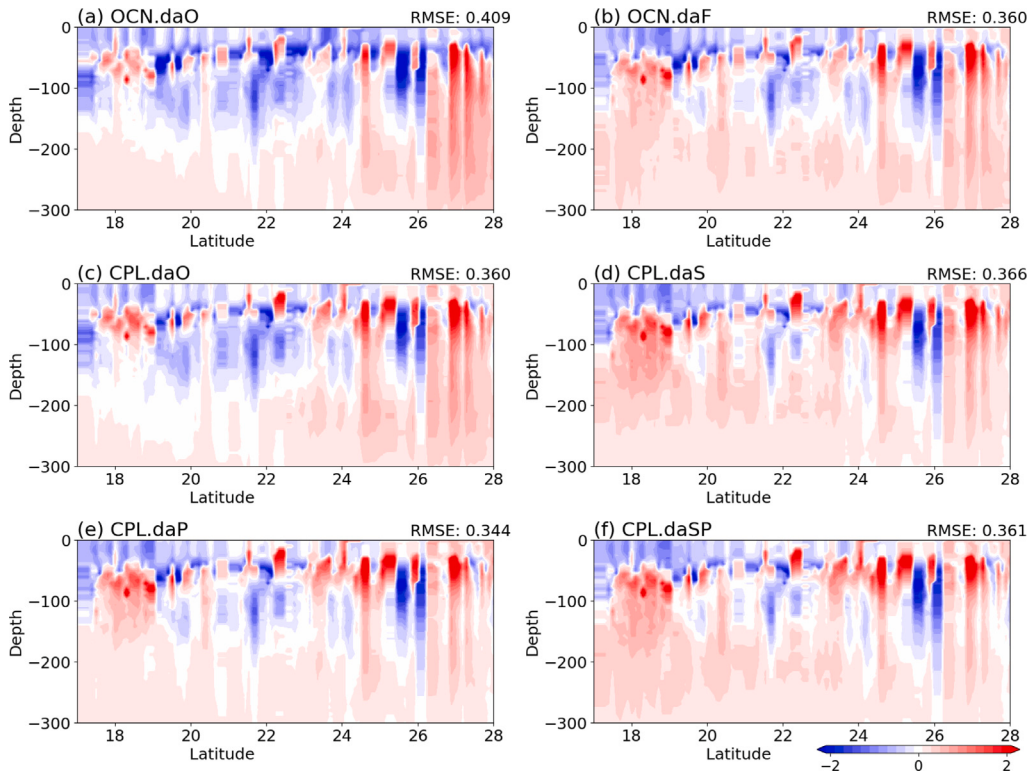


Fig. 9. The differences between the daily temperature at 0–300 m obtained in the DA experiments compared to in situ observations (results minus observations). The forecasts and the observations are collocated in space and time.

et al., 2010; Park et al., 2018). Here, we investigate the dynamical balances in our experiments by comparing the standard deviation of vertical current velocity w obtained in the DA experiments with the uncoupled and coupled “free” runs without assimilating observation data in Fig. 12. Larger standard deviation of w suggests spurious vertical speeds induced by imbalanced ocean states. The results in Fig. 12 show that the spreads of w in all DA experiments (CPL.daO, CPL.daS, CPL.daP, CPL.daSP) are larger than the “free” runs (OCN.free and CPL.free), indicating the ocean model are more imbalanced after assimilating the ocean observations. Because the changes in w spread in CPL.daSP are close to the ocean-only model experiment OCN.daF, we hypothesize that no significant dynamical imbalances are introduced when using the coupled model.

4. Summary and conclusions

This work implemented an EAKF data assimilation framework based on the regional coupled model SKRIPS and DART. We investigate the impact of ocean data assimilation on the oceanic and atmospheric states of the Red Sea. The coupled system assimilates satellite-based sea surface temperature and height and in situ temperature and salinity glider profiles every 3 days for 1 year starting from January 01, 2011.

To assess the performance of the ensemble forecasts and examine the generated ocean states, we ran a series of experiments using different perturbation schemes. The assimilation results of the coupled experiments are compared with the uncoupled ones forced by ECMWF-derived surface forcing, revealing that the coupled experiments give greater spread in the ensembles of ocean states, with the spread continuing to increase when using the stochastic kinetic energy backscatter (SKEB) scheme. Compared with the assimilated data, the coupled experiments result in a more skillful SST and SSH ensemble mean forecast. The SST forecasts and SSH analyses in coupled models

are also better than uncoupled ones when compared with the independent observational data, but the RMSEs of SST analyses and SSH forecasts are insignificantly different.

We further compared the DA experiment results with the independent cruise observation data of temperature and temperature profiles. The comparison shows large variations in the temperature profiles because of the challenge in modeling the thermocline layer and the lack of other in situ data. The RMSEs from the coupled DA experiments with perturbations of the atmospheric model are comparable to the uncoupled model driven by ECMWF-derived ensemble forcing, and both are better than the benchmark experiments with small spreads in atmospheric forcings. To investigate the feedback from the ocean, we validated the latent heat flux and 10 m winds in all coupled experiments using ERA5 data, but no significant difference is observed. Although the feedback from the ocean does not significantly change atmospheric states in the coupled experiments, the uncertainties of the atmosphere are likely to be better accounted for in the perturbed experiments. In addition, the RMSEs of the ensemble mean of the atmosphere forcing are mostly larger than the ensemble spread, indicating that the atmospheric ensembles are not excessively perturbed in this experiment.

This study demonstrates that our Red Sea DA system using two-way coupled model with WRF performs better or equal to an uncoupled model driven by ECMWF-derived ensemble surface forcing, showing a promising approach for forecasting the oceanic states or producing ocean analysis data. The dynamical imbalances in the coupled model are also not significantly different from the uncoupled model.

Future work will involve the assimilation of higher resolution satellite observation data and more in situ observations for the Red Sea region. The coupled effects on the forecast/analysis will also be explored and the reliability will be examined (e.g., Rodwell et al., 2016). The specific events that lead to large spread of SST and atmospheric

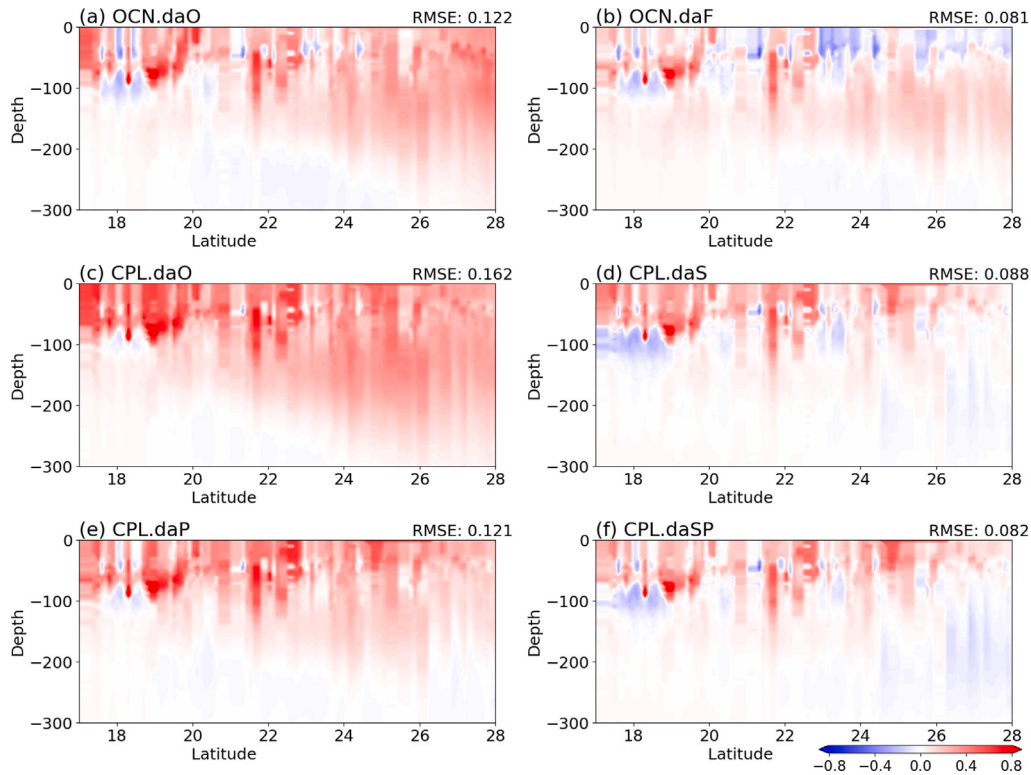


Fig. 10. The differences between the daily salinity at 0–300 m obtained in the DA experiments in comparison with in situ observations (results minus observations). The forecasts and the observations are collocated in space and time.

forcing due to the Tokar jets are to be investigated. We will further investigate the model physics options and the parameters being used in the experiments, especially for the coupled experiments. In addition, the covariance between different ocean states will be explored to better understand the physical insights of the ocean and the coupled effects.

CRediT authorship contribution statement

Rui Sun: Writing – original draft, Visualization, Validation, Software, Methodology, Investigation, Formal analysis, Conceptualization. **Sivareddy Sanikommu:** Writing – original draft, Software, Methodology, Investigation, Formal analysis, Data curation, Conceptualization. **Aneesh C. Subramanian:** Writing – review & editing, Supervision, Project administration, Methodology, Investigation, Formal analysis, Conceptualization. **Matthew R. Mazloff:** Writing – review & editing, Supervision, Project administration, Methodology, Investigation, Formal analysis, Conceptualization. **Bruce D. Cornuelle:** Writing – review & editing, Supervision, Project administration, Methodology, Investigation, Formal analysis, Conceptualization. **Ganesh Gopalakrishnan:** Writing – review & editing, Supervision, Project administration, Methodology, Investigation, Formal analysis, Conceptualization. **Arthur J. Miller:** Writing – review & editing, Supervision, Project administration, Methodology, Investigation, Formal analysis, Conceptualization. **Ibrahim Hoteit:** Writing – review & editing, Supervision, Resources, Project administration, Methodology, Funding acquisition, Conceptualization.

Declaration of competing interest

The authors declare that they have no known competing financial interests or personal relationships that could have appeared to influence the work reported in this paper.

Data availability

The coupled model used for the simulations is available at https://github.com/iurnus/scripps_kaust_model. The DA experimental results used in the paper are available at <https://zenodo.org/records/10408667>.

Acknowledgments

We gratefully acknowledge the research funding (grant number: OSR-2022-NCM-4829.5) from KAUST (King Abdullah University of Science and Technology), Saudi Arabia. We also appreciate the assistance provided by KAUST Supercomputer Laboratory and the computational resources of the supercomputer Shaheen II and III. RS and ACS were supported by ONR ASTRAL research initiative (N00014-23-1-2092). ACS was supported by NOAA Grant NA18OAR4310405 and ONR MIS-OBOB research initiative (N00014-17-S-B001). BDC and MRM were supported by NOAA Grant NA21OAR4310257, NA18OAR4310403, and NA22OAR4310597. AJM was partly supported by the National Science Foundation, United States (OCE-2022868). GG was supported by ONR funding N000142112726. We appreciate Luca Delle Monache, Alison Cobb, Daniel Steinhoff, and Rachel Weihs for discussing the generation of WRF ensembles.

Appendix A. Covariance of selected ocean states

Good background error covariance estimates are crucial to DA performance so it is useful to analyze them in detail. However it is not possible to visualize the full background error covariance matrix as it is very large (with a dimension of about $10^7 \times 10^7$ in our experiments). Instead we focus on a few important aspects of the background error covariance, in particular covariance model fields with selected points.

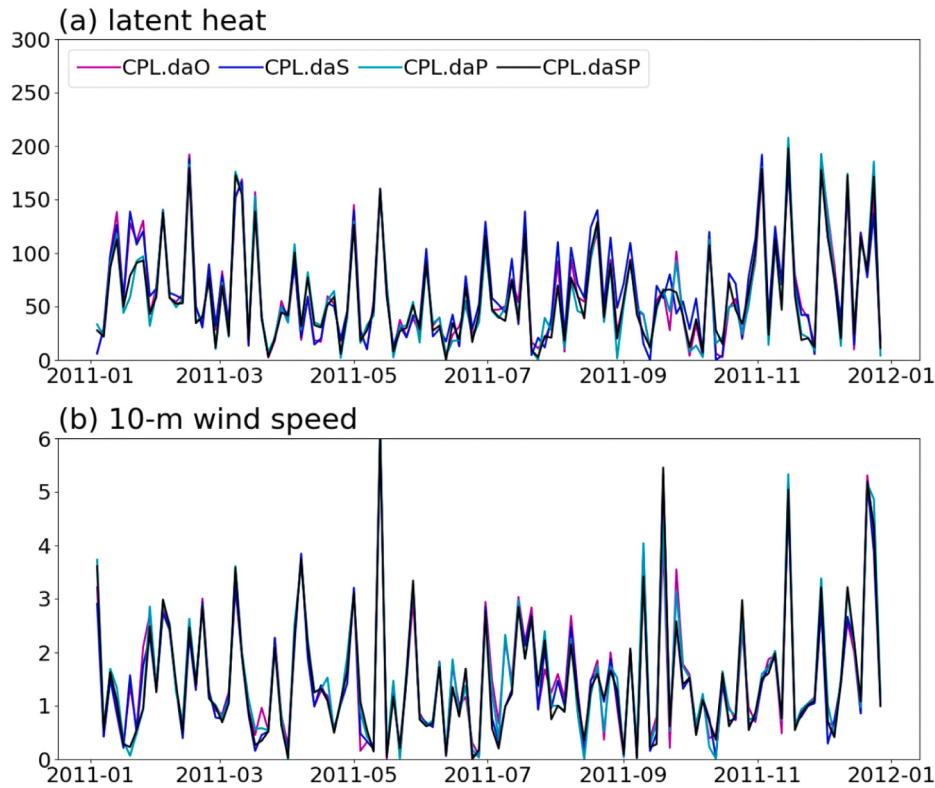


Fig. 11. The RMSEs of latent heat flux and 10-m wind speed obtained in the coupled model when assimilating the ocean data. Only the data on the centerline of the Red Sea are compared.

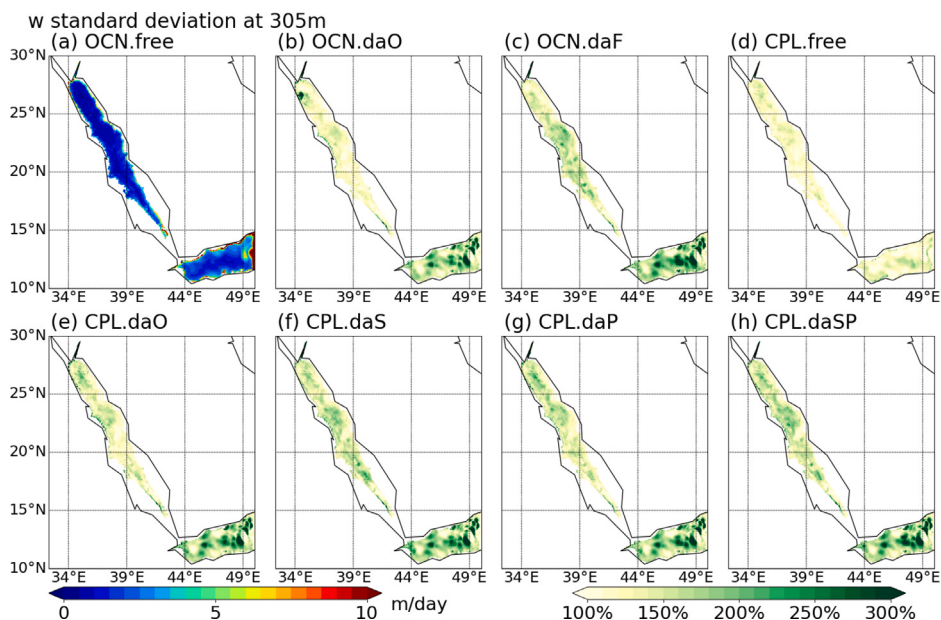


Fig. 12. Standard deviation of vertical current velocity w at 300 m obtained in the DA experiments. OCN.free and CPL.free are two “free” runs without assimilating observation data. Panels (b)–(h) are normalized by the reference OCN.free in panel (a) to highlight differences.

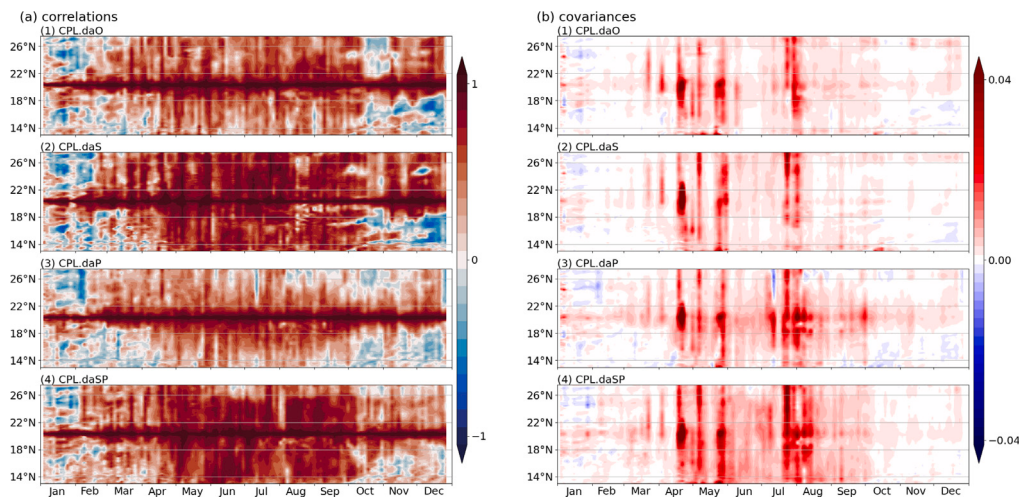


Fig. A.1. The correlations and covariances between the SST along the centerline of the Red Sea and the SST at 20.2°N, 39.0°E (the “center” of the line). Panels (1–4) show the correlations and covariances obtained in CPL.daO, CPL.daS, CPL.daP, and CPL.daSP, respectively.

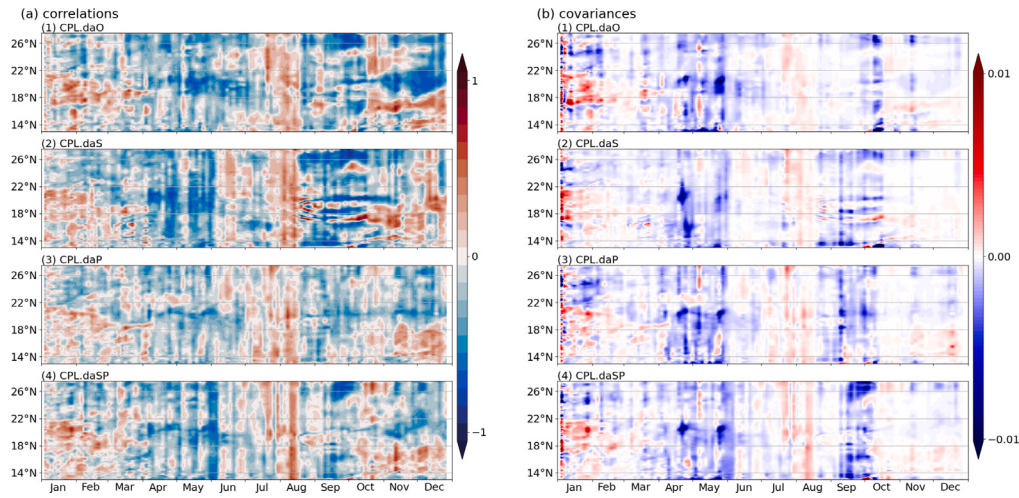


Fig. A.2. The correlations and covariances between the SST along the centerline of the Red Sea and the sea surface salinity at 20.2°N, 39.0°E (the “center” of the line). Panels (1–4) show the correlations and covariances obtained in CPL.daO, CPL.daS, CPL.daP, and CPL.daSP, respectively.

The covariance of the ocean states are shown in Figs. A.1 and A.2. Because it is not practical or feasible to output the entire model error covariance, we only present the covariance from the variables along the centerline of the Red Sea from the ensemble model forecasts. Fig. A.1 shows the correlation and covariance between the SST along the centerline of the Red Sea and the SST at the center point (20.2°N, 39.0°E). The correlation in Fig. A.1(a) has higher values along the center and lower values away from the center, indicating the SST in the north or south Red Sea is less correlated with the SST at the center. The covariance in Fig. A.1(b) also has larger values along the center, and the covariance is larger in summer due to larger SST variances during this time (covariance is the product of correlation and variance). From the comparison of the DA experiments using different schemes to perturb the atmospheric forcing, it can be seen that CPL.daSP has the largest SST covariance. This is consistent with the SST spread shown in Fig. 4. In our manuscript we focus discuss on ensemble spread, as is commonly done in previous literature (Hoteit et al., 2013; Sanikommu et al., 2020). Though not guaranteed to be true, the ensemble spread is assumed to be a proxy for covariance structure and magnitude in the ensemble.

Fig. A.2 shows the correlations and covariances between the SST along the centerline of the Red Sea and the sea surface salinity at the center point (20.2°N, 39.0°E). In Fig. A.2(b) the covariance of

CPL.daSP is also larger than other experiments, indicating the increase of atmospheric forcing spread also increases the spread of the covariance between different variables. This indicates that the increase of atmospheric forcing spread also increases the spread of the covariance between different variables and remains to be investigated in the future work. In addition, the covariance plot shows the spurious correlation of the variables at larger scale and the necessity of using a cut off radius of 300 km for localization.

Appendix B. Relative differences of temperature and salinity profiles

The relative differences of the temperature and salinity profiles obtained from the experiments are shown in Figs. B.1 and B.2. This is to highlight the relative improvements from the coupled runs using different schemes to perturb the atmospheric forcing. Figs. B.1(a) and B.2(a) show the bias of the temperature and salinity obtained in OCN.daO compared from the in situ observation. The other panels are the relative differences, with the color indicating the increase or decrease of the absolute bias. The CPL.daSP has a smaller bias near the surface between 0 to 20 m, and this is consistent with the RMSEs shown in Fig. 6. It can be seen that the temperature and salinity profiles obtained in CPL.daSP have less bias between 22 to 28°N where the validation profiles are closer to the assimilated EN4 data.

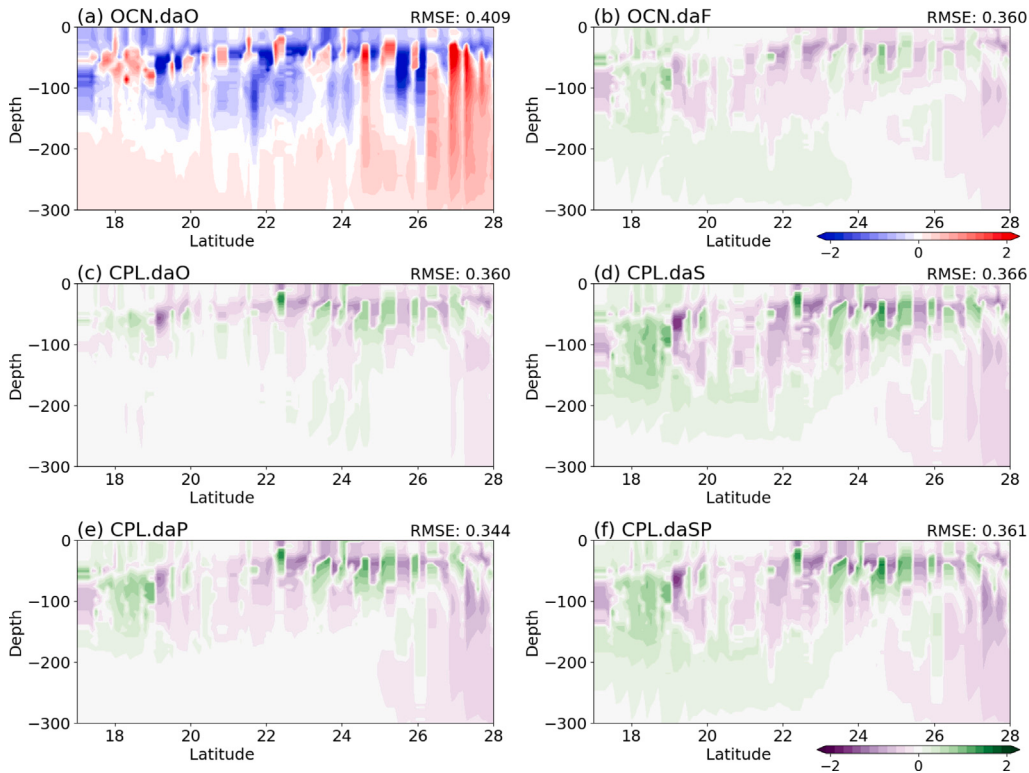


Fig. B.1. The differences between the daily temperature at 0–300 m obtained in the DA experiments compared to in situ observations. The forecasts and the observations are collocated in space and time. Panel (a) shows the bias (results minus observations) between OCN.daO and the in situ observation; Panels (b–f) are the relative differences, with the color indicating the increase or decrease of the absolute bias.

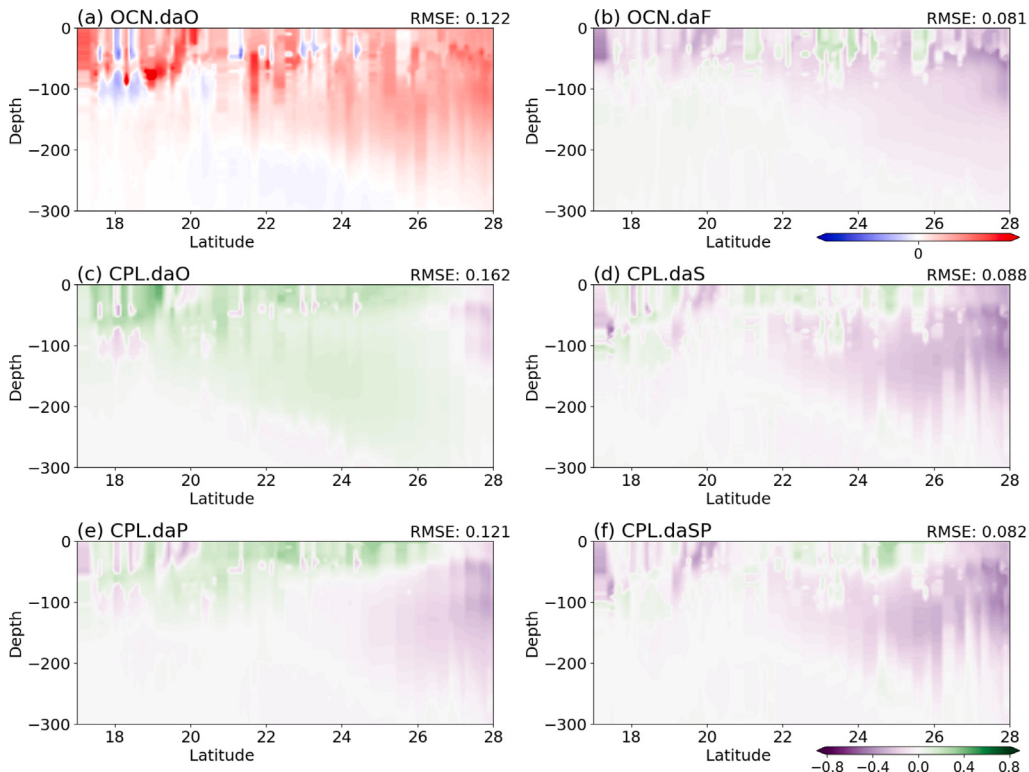


Fig. B.2. The differences between the daily salinity at 0–300 m obtained in the DA experiments in comparison with in situ observations. The forecasts and the observations are collocated in space and time. Panel (a) shows the bias (results minus observations) between OCN.daO and the in situ observation; Panels (b–f) are the relative differences, with the color indicating the increase or decrease of the absolute bias.

References

- Anderson, J.L., 2001. An ensemble adjustment Kalman filter for data assimilation. *Mon. Weather Rev.* 129 (12), 2884–2903.
- Anderson, J., Anderson, S., 1999. A Monte Carlo implementation of the nonlinear filtering problem to produce ensemble assimilations and forecasts. *Mon. Weather Rev.* 127 (12), 2741–2758.
- Anderson, J., Hoar, T., Raeder, K., Liu, H., Collins, N., Torn, R., Avellano, A., 2009. The data assimilation research testbed: A community facility. *Bull. Am. Meteorol. Soc.* 90 (9), 1283–1296.
- Anderson, L.A., Robinson, A.R., Lozano, C.J., 2000. Physical and biological modeling in the Gulf Stream region: I. Data assimilation methodology. *Deep Sea Res. I: Oceanogr. Res. Pap.* 47 (10), 1787–1827.
- Bannister, R.N., 2008a. A review of forecast error covariance statistics in atmospheric variational data assimilation. I: Characteristics and measurements of forecast error covariances. *Q. J. R. Meteorol. Soc.* 134 (637, B), 1951–1970.
- Bannister, R.N., 2008b. A review of forecast error covariance statistics in atmospheric variational data assimilation. II: Modelling the forecast error covariance statistics. *Q. J. R. Meteorol. Soc.* 134 (637), 1971–1996.
- Bannister, R.N., 2017. A review of operational methods of variational and ensemble-variational data assimilation. *Q. J. R. Meteorol. Soc.* 143 (703), 607–633.
- Banzon, V., Smith, T.M., Chin, T.M., Liu, C., Hankins, W., 2016. A long-term record of blended satellite and in situ sea-surface temperature for climate monitoring, modeling and environmental studies. *Earth Syst. Sci. Data* 8 (1), 165–176.
- Berner, J., Fossel, K., Ha, S.-Y., Hacker, J., Snyder, C., 2015. Increasing the skill of probabilistic forecasts: Understanding performance improvements from model-error representations. *Mon. Weather Rev.* 143 (4), 1295–1320.
- Berner, J., Ha, S.-Y., Hacker, J., Fournier, A., Snyder, C., 2011. Model uncertainty in a mesoscale ensemble prediction system: Stochastic versus multiphysics representations. *Mon. Weather Rev.* 139 (6), 1972–1995.
- Berner, J., Shutts, G., Leutbecher, M., Palmer, T., 2009. A spectral stochastic kinetic energy backscatter scheme and its impact on flow-dependent predictability in the ECMWF ensemble prediction system. *J. Atmos. Sci.* 66 (3), 603–626.
- Bougeault, P., Toth, Z., Bishop, C., Brown, B., Burridge, D., Chen, D.H., Ebert, B., Fuentes, M., Hamill, T.M., Mylne, K., et al., 2010. The THORPEX interactive grand global ensemble. *Bull. Am. Meteorol. Soc.* 91 (8), 1059–1072.
- Brankart, J.-M., Candille, G., Garnier, F., Calone, C., Melet, A., Bouttier, P.-A., Brasseur, P., Verron, J., 2015. A generic approach to explicit simulation of uncertainty in the NEMO ocean model. *Geosci. Model Dev.* 8 (5), 1285–1297.
- Buizza, R., 2014. The TIGGE Global, Medium-Range Ensembles. European Centre for Medium-Range Weather Forecasts.
- Chen, S.-H., Sun, W.-Y., 2002. A one-dimensional time dependent cloud model. *J. Meteorol. Soc. Japan Ser. II* 80 (1), 99–118.
- Cox, M., 1987. Isopycnal diffusion in a z-coordinate ocean model. *Ocean Model.* 74, 1–5.
- Danabasoglu, G., McWilliams, J., 1995. Sensitivity of the global ocean circulation to parameterizations of mesoscale tracer transports. *J. Clim.* 8 (12), 2967–2987.
- Dasari, H.P., Desamsetti, S., Langodan, S., Attada, R., Ashok, K., Hoteit, I., 2021. Long-term changes in the Arabian Peninsula rainfall and their relationship with the ENSO signals in the tropical Indo-Pacific. *Clim. Dyn.* 1–17.
- Davis, S.R., Farrar, J.T., Weller, R.A., Jiang, H., Pratt, L.J., 2019. The land-sea breeze of the Red Sea: observations, simulations, and relationships to regional moisture transport. *J. Geophys. Res.: Atmos.* 124 (24), 13803–13825.
- Donlon, C.J., Martin, M., Stark, J., Roberts-Jones, J., Fiedler, E., Wimmer, W., 2012. The operational sea surface temperature and sea ice analysis (OSTIA) system. *Remote Sens. Environ.* 116, 140–158.
- ECMWF, 2017. ERA5 Data Documentation. Tech. Rep., European Center for Medium-Range Weather Forecasts.
- Edwards, C.A., Moore, A.M., Hoteit, I., Cornuelle, B.D., 2015. Regional ocean data assimilation. In: Carlson, C., Giovannoni, S. (Eds.), *Annual Review of Marine Science*, Vol. 7. In: *Annual Review of Marine Science*, vol. 7, pp. 21–42.
- Evensen, G., 1994. Sequential data assimilation with a nonlinear quasi-geostrophic model using Monte Carlo methods to forecast error statistics. *J. Geophys. Res.: Oceans* 99 (C5), 10143–10162.
- Evensen, G., 2003. The ensemble Kalman filter: Theoretical formulation and practical implementation. *Ocean Dyn.* 53, 343–367.
- Evensen, G., 2004. Sampling strategies and square root analysis schemes for the EnKF. *Ocean Dyn.* 54 (6), 539–560.
- Evensen, G., Van Leeuwen, P.J., 1996. Assimilation of Geosat altimeter data for the Agulhas current using the ensemble Kalman filter with a quasigeostrophic model. *Mon. Weather Rev.* 124 (1), 85–96.
- Fairall, C., Bradley, E.F., Hare, J., Grachev, A., Edson, J., 2003. Bulk parameterization of air-sea fluxes: Updates and verification for the COARE algorithm. *J. Clim.* 16 (4), 571–591.
- Gaspar, P., Gregoris, Y., Lefevre, J., 1990. A simple eddy kinetic-energy model for simulations of the oceanic vertical mixing - tests at station papa and long-term upper ocean study site. *J. Geophys. Res. Oceans* 95 (C9), 16179–16193.
- Gent, P., McWilliams, J., 1990. Isopycnal mixing in ocean circulation models. *J. Phys. Oceanogr.* 20 (1), 150–155.
- Gent, P., Willebrand, J., McDougall, T., McWilliams, J., 1995. Parameterizing eddy-induced tracer transports in ocean circulation models. *J. Phys. Oceanogr.* 25 (4), 463–474.
- Good, S.A., Martin, M.J., Rayner, N.A., 2013. EN4: Quality controlled ocean temperature and salinity profiles and monthly objective analyses with uncertainty estimates. *J. Geophys. Res.: Oceans* 118 (12), 6704–6716.
- Grell, G.A., Freitas, S.R., 2014. A scale and aerosol aware stochastic convective parameterization for weather and air quality modeling. *Atmos. Chem. Phys.* 14 (10), 5233–5250.
- Griffies, S., Hallberg, R., 2000. Biharmonic friction with a Smagorinsky-like viscosity for use in large-scale eddy-permitting ocean models. *Mon. Weather Rev.* 128 (8, 2), 2935–2946.
- Harrop, C., Trahan, S., Holt, C., Brown, T., 2017. Rocoto 1.2.4. <http://dx.doi.org/10.5281/zenodo.890939>.
- Hill, C., DeLuca, C., Balaji, Suarez, M., Silva, A., 2004. The architecture of the earth system modeling framework. *Comput. Sci. Eng.* 6 (1), 18–28.
- Holland, W., 1978. Role of mesoscale eddies in general circulation of ocean - numerical experiments using a wind-driven quasi-geostrophic model. *J. Phys. Oceanogr.* 8 (3), 363–392.
- Hong, S.-Y., Lim, J.-O.J., 2006. The WRF single-moment 6-class microphysics scheme (WSM6). *Asia-Pac. J. Atmos. Sci.* 42 (2), 129–151.
- Hong, S.-Y., Noh, Y., Dudhia, J., 2006. A new vertical diffusion package with an explicit treatment of entrainment processes. *Mon. Weather Rev.* 134 (9), 2318–2341.
- Hoteit, I., Abualnaja, Y., Afzal, S., Ait-El-Fquih, B., Akyolas, T., Antony, C., Dawson, C., Asfahani, K., Brewin, R.J., Cavalieri, L., Cerovecki, I., Cornuelle, B., Desamsetti, S., Attada, R., Dasari, H., Sanchez-Garrido, J., Genevier, L., Gharamti, M.E., Gittings, J.A., Gokul, E., Gopalakrishnan, G., Guo, D., Hadri, B., Hadwiger, M., Hammoud, M.A., Hendershott, M., Hittawę, M., Karumuri, A., Knio, O., Köhl, A., Kortas, S., Krokos, G., Kunchala, R., Issa, L., Lakkis, I., Langodan, S., Lermusiaux, P., Luong, T., Ma, J., Maitre, O.L., Mazloff, M., Mohtar, S.E., Papadopoulos, V.P., Platt, T., Pratt, L., Raboudi, N., Racault, M.-F., Raitsos, D.E., Razak, S., Sanikommu, S., Sathyendranath, S., Sofianos, S., Subramanian, A., Sun, R., Titi, E., Toye, H., Triantafyllou, G., Tsiaras, K., Vasou, P., Viswanadhapalli, Y., Wang, Y., Yao, F., Zhan, P., Zodiatis, G., 2021. Towards an end-to-end analysis and prediction system for weather, climate, and marine applications in the Red Sea. *Bull. Am. Meteorol. Soc.* 102 (1), E99 – E122. <http://dx.doi.org/10.1175/BAMS-D-19-0005.1>, Retrieved from <https://journals.ametsoc.org/view/journals/bams/102/1/BAMS-D-19-0005.1.xml>.
- Hoteit, I., Cornuelle, B., Heimbach, P., 2010. An eddy-permitting, dynamically consistent adjoint-based assimilation system for the tropical Pacific: Hindcast experiments in 2000. *J. Geophys. Res.: Oceans* 115 (C3).
- Hoteit, I., Hoar, T., Gopalakrishnan, G., Collins, N., Anderson, J., Cornuelle, B., Köhl, A., Heimbach, P., 2013. A MITgcm/DART ensemble analysis and prediction system with application to the Gulf of Mexico. *Dyn. Atmos. Oceans* 63, 1–23.
- Hoteit, I., Pham, D., Blum, J., 2002. A simplified reduced order Kalman filtering and application to altimetric data assimilation in Tropical Pacific. *J. Mar. Syst.* 36 (1–2), 101–127.
- Hoteit, I., Pham, D.-T., Gharamti, M., Luo, X., 2015. Mitigating observation perturbation sampling errors in the stochastic EnKF. *Mon. Weather Rev.* 143 (7), 2918–2936.
- Houtekamer, P.L., Mitchell, H.L., Pellerin, G., Buehner, M., Charron, M., Spacek, L., Hansen, B., 2005. Atmospheric data assimilation with an ensemble Kalman filter: Results with real observations. *Mon. Weather Rev.* 133 (3), 604–620.
- Iacono, M.J., Delamere, J.S., Mlawer, E.J., Shephard, M.W., Clough, S.A., Collins, W.D., 2008. Radiative forcing by long-lived greenhouse gases: Calculations with the AER radiative transfer models. *J. Geophys. Res.: Atmos.* 113 (D13).
- Ingleby, B., Huddleston, M., 2007. Quality control of ocean temperature and salinity profiles—Historical and real-time data. *J. Mar. Syst.* 65 (1–4), 158–175.
- Janjić, Z.I., 1994. The step-mountain eta coordinate model: Further developments of the convection, viscous sublayer, and turbulence closure schemes. *Mon. Weather Rev.* 122 (5), 927–945.
- Jean-Michel, L., Eric, G., Romain, B.-B., Gilles, G., Angélique, M., Marie, D., Clément, B., Mathieu, H., Olivier, L.G., Charly, R., et al., 2021. The copernicus global 1/12 oceanic and sea ice GLORYS12 reanalysis. *Front. Earth Sci.* 9, 698876.
- Kain, J.S., 2004. The Kain-Fritsch convective parameterization: an update. *J. Appl. Meteorol.* 43 (1), 170–181.
- Karnaustas, K.B., Jones, B.H., 2018. The interannual variability of sea surface temperature in the Red Sea from 35 years of satellite and in situ observations. *J. Geophys. Res.: Oceans* 123 (8), 5824–5841.
- Karspeck, A.R., Yeager, S., Danabasoglu, G., Hoar, T., Collins, N., Raeder, K., Anderson, J., Tribbia, J., 2013. An ensemble adjustment Kalman filter for the CCSM4 ocean component. *J. Clim.* 26 (19), 7392–7413.
- Kwon, K.M., Choi, B.-J., Lee, S.-H., Kim, Y.H., Seo, G.-H., Cho, Y.-K., 2016. Effect of model error representation in the Yellow and East China Sea modeling system based on the ensemble Kalman filter. *Ocean Dyn.* 66 (2), 263–283.
- Kwon, Y.C., Hong, S.-Y., 2017. A mass-flux cumulus parameterization scheme across gray-zone resolutions. *Mon. Weather Rev.* 145 (2), 583–598.
- Langodan, S., Cavalieri, L., Vishwanadhapalli, Y., Pomaro, A., Bertotti, L., Hoteit, I., 2017. The climatology of the Red Sea-part 1: the wind. *Int. J. Climatol.* 37 (13), 4509–4517.

- Large, W., Danabasoglu, G., Doney, S., McWilliams, J., 1997. Sensitivity to surface forcing and boundary layer mixing in a global ocean model: Annual-mean climatology. *J. Phys. Oceanogr.* 27 (11), 2418–2447.
- Large, W.G., McWilliams, J.C., Doney, S.C., 1994. Oceanic vertical mixing: A review and a model with a nonlocal boundary layer parameterization. *Rev. Geophys.* 32 (4), 363–403.
- Lawson, W., Hansen, J., 2004. Implications of stochastic and deterministic filters as ensemble-based data assimilation methods in varying regimes of error growth. *Mon. Weather Rev.* 132 (8), 1966–1981.
- Leeuwenburgh, O., Evensen, G., Bertino, L., 2005. The impact of ensemble filter definition on the assimilation of temperature profiles in the tropical Pacific. *Q. J. R. Meteorol. Soc.* 131 (613, C), 3291–3300.
- Leith, C., 1996. Stochastic models of chaotic systems. *Phys. D* 98 (2–4), 481–491, 15th Annual International Conference of the Center-for-Nonlinear-Studies on Nonlinear Phenomena in Ocean Dynamics, Los Alamos, NM, MAY 15-19, 1995.
- Lim, K.-S.S., Hong, S.-Y., 2010. Development of an effective double-moment cloud microphysics scheme with prognostic cloud condensation nuclei (CCN) for weather and climate models. *Mon. Weather Rev.* 138 (5), 1587–1612.
- Lima, L.N., Pezzi, L.P., Penny, S.G., Tanajura, C.A.S., 2019. An investigation of ocean model uncertainties through ensemble forecast experiments in the southwest Atlantic Ocean. *J. Geophys. Res. Oceans* 124 (1), 432–452.
- Lisæter, K.A., Rosanova, J., Evensen, G., 2003. Assimilation of ice concentration in a coupled ice-ocean model, using the ensemble Kalman filter. *Ocean Dyn.* 53 (4), 368–388.
- Liu, P., Tsimpidi, A., Hu, Y., Stone, B., Russell, A., Nenes, A., 2012. Differences between downscaling with spectral and grid nudging using WRF. *Atmos. Chem. Phys.* 12 (8), 3601–3610.
- Luo, X., Hoteit, I., 2012. Ensemble Kalman filtering with residual nudging. *Tellus A* 64 (1), 17130.
- Marshall, J., Adcroft, A., Hill, C., Perelman, L., Heisey, C., 1997. A finite-volume, incompressible Navier Stokes model for studies of the ocean on parallel computers. *J. Geophys. Res.: Oceans* 102 (C3), 5753–5766.
- Mellor, G., Yamada, T., 1982. Development of a turbulence closure-model for geophysical fluid problems. *Rev. Geophys.* 20 (4), 851–875.
- Mertz, F., Rosmorduc, V., Maheu, C., Faugére, Y., 2017. Product user manual, for sea level SLA products.
- Morrison, H., Thompson, G., Tatarkii, V., 2009. Impact of cloud microphysics on the development of trailing stratiform precipitation in a simulated squall line: Comparison of one-and two-moment schemes. *Mon. Weather Rev.* 137 (3), 991–1007.
- Nakanishi, M., Niino, H., 2004. An improved Mellor-Yamada level-3 model with condensation physics: Its design and verification. *Bound.-Layer Meteorol.* 112 (1), 1–31.
- Nakanishi, M., Niino, H., 2009. Development of an improved turbulence closure model for the atmospheric boundary layer. *J. Meteorol. Soc. Japan Ser. II* 87 (5), 895–912.
- Oakley, N.S., Liu, T., McGuire, L.A., Simpson, M., Hatchett, B.J., Tardy, A., Kean, J.W., Castellano, C., Laber, J.L., Steinhoff, D., 2023. Toward probabilistic post-fire debris-flow hazard decision support. *Bull. Am. Meteorol. Soc.*
- Pacanowski, R., Philander, S., 1981. Parameterization of vertical mixing in numerical models of tropical oceans. *J. Phys. Oceanogr.* 11 (11), 1443–1451.
- Park, J.-Y., Stock, C.A., Yang, X., Dunne, J.P., Rosati, A., John, J., Zhang, S., 2018. Modeling global ocean biogeochemistry with physical data assimilation: a pragmatic solution to the equatorial instability. *J. Adv. Modelling Earth Syst.* 10 (3), 891–906.
- Penny, S.G., Behringer, D.W., Carton, J.A., Kalnay, E., 2015. A hybrid global ocean data assimilation system at NCEP. *Mon. Weather Rev.* 143 (11), 4660–4677.
- Prakash, P.J., Stenckiv, G., Kalenderski, S., Osipov, S., Bangalath, H., 2014. The impact of dust storms on the Arabian Peninsula and the Red Sea. *Atmos. Chem. Phys. Discuss.* 14 (13).
- Redi, M., 1982. Oceanic isopycnal mixing by coordinate rotation. *J. Phys. Oceanogr.* 12 (10), 1154–1158.
- Reynolds, R.W., Smith, T.M., Liu, C., Chelton, D.B., Casey, K.S., Schlax, M.G., 2007. Daily high-resolution-blended analyses for sea surface temperature. *J. Clim.* 20 (22), 5473–5496.
- Rodwell, M., Lang, S., Ingleby, N., Bormann, N., Hölm, E., Rabier, F., Richardson, D., Yamaguchi, M., 2016. Reliability in ensemble data assimilation. *Q. J. R. Meteorol. Soc.* 142 (694), 443–454.
- Sakov, P., Counillon, F., Bertino, L., Lisæter, K., Oke, P., Koralev, A., 2012. TOPAZ4: an ocean-sea ice data assimilation system for the North Atlantic and Arctic. *Ocean Sci.* 8 (4), 633–656.
- Sandery, P.A., Sakov, P., Majewski, L., 2014. The impact of open boundary forcing on forecasting the east Australian current using ensemble data assimilation. *Ocean Model.* 84, 1–11.
- Sanikommu, S., Banerjee, D.S., Baduru, B., Paul, B., Paul, A., Chakraborty, K., Hoteit, I., 2019. Impact of dynamical representational errors on an Indian ocean ensemble data assimilation system. *Q. J. R. Meteorol. Soc.* 145 (725), 3680–3691.
- Sanikommu, S., Langodan, S., Dasari, H.P., Zhan, P., Kroks, G., Abuallnaja, Y.O., Asfahani, K., Hoteit, I., 2023a. Making the case for high-resolution regional ocean reanalyses: An example with the Red Sea. *Bull. Am. Meteorol. Soc.* 104 (7), E1241 – E1264. <http://dx.doi.org/10.1175/BAMS-D-21-0287.1>, Retrieved from <https://journals.ametsoc.org/view/journals/bams/104/7/BAMS-D-21-0287.1.xml>.
- Sanikommu, S., Paul, A., Sluka, T., Ravichandran, M., Kalnay, E., 2017. The pre-argo ocean reanalyses may be seriously affected by the spatial coverage of moored buoys. *Sci. Rep.* 7.
- Sanikommu, S., Raboudi, N., El Gharamti, M., Zhan, P., Hadri, B., Hoteit, I., 2023b. Insights from very-large-ensemble data assimilation experiments with a high-resolution general circulation model of the Red Sea. *Q. J. R. Meterol. Soc.*
- Sanikommu, S., Toye, H., Zhan, P., Langodan, S., Kroks, G., Knio, O., Hoteit, I., 2020. Impact of atmospheric and model physics perturbations on a high-resolution ensemble data assimilation system of the Red Sea. *J. Geophys. Res.: Oceans* 125 (8), e2019JC015611.
- Shu, Y., Zhu, J., Wang, D., Xiao, X., 2011. Assimilating remote sensing and in situ observations into a coastal model of northern South China Sea using ensemble Kalman filter. *Cont. Shelf Res.* 31 (6, S, SI), S24–S36.
- Shutts, G., 2005. A kinetic energy backscatter algorithm for use in ensemble prediction systems. *Q. J. R. Meteorol. Soc.* 131 (612), 3079–3102.
- Skamarock, W.C., Klemp, J.B., Dudhia, J., Gill, D.O., Liu, Z., Berner, J., Wang, W., Powers, J.G., Duda, M.G., Barker, D.M., et al., 2019. A Description of the Advanced Research WRF Model Version 4. Vol. 145, National Center for Atmospheric Research, Boulder, CO, USA, p. 550, (145).
- Smagorinsky, J., Galperin, B., Orszag, S., 1993. Large eddy simulation of complex engineering and geophysical flows. *Evol. Phys. Oceanogr.* 3–36.
- Song, H., Hoteit, I., Cornuelle, B.D., Subramanian, A.C., 2010. An adaptive approach to mitigate background covariance limitations in the ensemble Kalman filter. *Mon. Weather Rev.* 138 (7), 2825–2845.
- Stark, J.D., Donlon, C.J., Martin, M.J., McCulloch, M.E., 2007. OSTIA: An operational, high resolution, real time, global sea surface temperature analysis system. In: *Oceans 2007-Europe*. IEEE, pp. 1–4.
- Sun, R., Cobb, A., Villas Bôas, A.B., Langodan, S., Subramanian, A.C., Mazloff, M.R., Cornuelle, B.D., Miller, A.J., Pathak, R., Hoteit, I., 2023. Waves in SKRIPS: WAVEWATCH III coupling implementation and a case study of tropical cyclone Mekunu. *Geosci. Model Dev.* 16 (12), 3435–3458.
- Sun, R., Subramanian, A.C., Miller, A.J., Mazloff, M.R., Hoteit, I., Cornuelle, B.D., 2019. SKRIPS v1.0: A regional coupled ocean-atmosphere modeling framework (MITgcm-WRF) using ESMF/NUOPC, description and preliminary results for the Red Sea. *Geosci. Model Dev.* 12 (10), 4221–4244. <http://dx.doi.org/10.5194/gmd-12-4221-2019>.
- Tewari, M., Chen, F., Wang, W., Dudhia, J., LeMone, M., Mitchell, K., Ek, M., Gayno, G., Wegiel, J., Cuenca, R., 2004. Implementation and verification of the unified NOAH land surface model in the WRF model. In: *20th Conference on Weather Analysis and Forecasting/16th Conference on Numerical Weather Prediction*. Vol. 1115, American Meteorological Society Seattle, WA.
- Thompson, G., Field, P.R., Rasmussen, R.M., Hall, W.D., 2008. Explicit forecasts of winter precipitation using an improved bulk microphysics scheme. Part II: Implementation of a new snow parameterization. *Mon. Weather Rev.* 136 (12), 5095–5115.
- Toye, H., Zhan, P., Gopalakrishnan, G., Kartadikaria, A.R., Huang, H., Knio, O., Hoteit, I., 2017. Ensemble data assimilation in the Red Sea: sensitivity to ensemble selection and atmospheric forcing. *Ocean Dyn.* 67 (7), 915–933.
- Vandenbulcke, L., Barth, A., 2015. A stochastic operational forecasting system of the Black Sea: Technique and validation. *Ocean Model.* 93, 7–21.
- Wan, L., Zhu, J., Bertino, L., Wang, H., 2008. Initial ensemble generation and validation for ocean data assimilation using HYCOM in the Pacific. *Ocean Dyn.* 58, 81–99.
- Whitaker, J.S., Hamill, T.M., 2012. Evaluating methods to account for system errors in ensemble data assimilation. *Mon. Weather Rev.* 140 (9), 3078–3089.
- Zhai, P., Bower, A.S., Smethie, Jr., W.M., Pratt, L.J., 2015. Formation and spreading of Red Sea outflow water in the Red Sea. *J. Geophys. Res.: Oceans* 120 (9), 6542–6563.
- Zhang, F., Snyder, C., Sun, J., 2004. Impacts of initial estimate and observation availability on convective-scale data assimilation with an ensemble Kalman filter. *Mon. Weather Rev.* 132 (5), 1238–1253.
- Zhang, C., Wang, Y., 2017. Projected future changes of tropical cyclone activity over the western north and South Pacific in a 20-km-mesh regional climate model. *J. Clim.* 30 (15), 5923–5941.